# Rh/CeO$_2$ Thin Catalytic Layer Deposition on Alumina Foams: Catalytic Performance and Controlling Regimes in Biogas Reforming Processes

**Cristina Italiano [1],\*, Muhammad Arsalan Ashraf [2]** [ID]**, Lidia Pino [1]** [ID]**,
Carmen Williana Moncada Quintero [3], Stefania Specchia [1,3]** [ID] **and Antonio Vita [1]**

[1]   CNR-ITAE, Institute for Advanced Energy Technologies "Nicola Giordano", Via S. Lucia sopra Contesse 5,
    98126 Messina, Italy; lidia.pino@itae.cnr.it (L.P.); stefania.specchia@polito.it (S.S.);
    antonio.vita@itae.cnr.it (A.V.)
[2]   Department of Chemical Engineering, University of Bath, Claverton Down Rd., Bath BA2 7AY, UK;
    m.a.ashraf@bath.ac.uk
[3]   Department of Applied Science and Technology, Politecnico di Torino, Corso Duca degli Abruzzi 24,
    10129 Torino, Italy; carmen.moncada@polito.it
\*   Correspondence: cristina.italiano@itae.cnr.it; Tel.: +39-090-624-927

[check for updates]

**Abstract:** The application of ceramic foams as structured catalyst supports is clearly expanding due to faster mass/heat transfer and higher contact efficiency than honeycomb monoliths and, mainly, packed beds. In this paper, alumina open-cell foams (OCFs) with different pore density (20, 30 and 40 ppi) were coated with Rh/CeO$_2$ catalyst via a two steps synthesis method involving: (i) the solution combustion synthesis (SCS) to in-situ deposit the CeO$_2$ carrier and (ii) the wet impregnation (WI) of the Rh active phase. The catalytic coatings were characterized in terms of morphology and adhesion properties by SEM/EDX analysis and ultrasounds test. Permeability and form coefficient were derived from pressure drop data. Catalytic performance was evaluated towards biogas Steam Reforming (SR) and Oxy-Steam Reforming (OSR) processes at atmospheric pressure by varying temperature (800–900 °C) and space velocity (35,000–140,000 NmL·g$^{-1}$·h$^{-1}$). Characteristics time analysis and dimensionless numbers were calculated to identify the controlling regime. Stability tests were performed for both SR and OSR over 200 h of time-on-stream (TOS) through consecutive start-up and shut-down cycles. As a result, homogenous, thin and high-resistance catalytic layers were in situ deposited on foam struts. All structured catalysts showed high activity, following the order 20 ppi < 30 ppi ≈ 40 ppi. External interphase (gas-solid) and external diffusion can be improved by reducing the pore diameter of the OCF structures. Anderson criterion revealed the absence of internal heat transfer resistances, as well as Damköhler and Weisz-Prater numbers excluded any internal mass transfer controlling regime, mainly due to thin coating thickness provided by the SCS method. Good stability was observed over 200 h of TOS for both SR and OSR processes.

**Keywords:** open-cell foam; structured catalyst; solution combustion synthesis; steam and oxy-steam reforming; process intensification
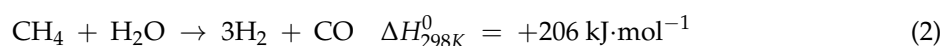
## 1. Introduction

Bio-economy is a sustainable solution to meet the challenges of food security, resource scarcity, energy demand and climate change by efficient production of bio-resources and their conversion into food, bio-energy and biomaterials [1]. Process intensification (PI) is a promising strategy to develop more competitive and sustainable processes in a transition towards a bio-based economy. The innovative methodologies of PI are exploited to overcome limitations of conventional

processes and develop novel processes by implementing efficient technologies that is, novel reactors, materials, separation processes, bio-materials and bio-based process routes [2,3]. The most interesting technological approach in heterogeneous catalysis is the application of structured catalysts (e.g., monoliths and foams) which paves a way for more energy and resources through efficient chemical transformations [4,5]. Monolith- and foam-structured catalysts are widely used in environmental applications for controlling both automotive and stationary emissions [6]. Moreover, they are increasingly under development for many reaction applications, such as highly endothermic and exothermic reactions (hydrogenation, combustion or reforming processes) especially at low contact time [7,8].
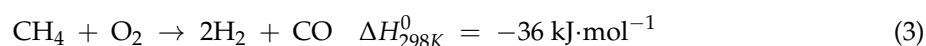
Biogas plays a major role as a renewable energy source in the bio-economy domain according to the European Union policy [9,10]. Biogas is produced by anaerobic digestion of biomasses coming from different sources such as sewage, sludge, landfill, or industry [11]. Basically, it consists of 50–75% $CH_4$, 25–45% $CO_2$, 2–7% $H_2O$ (at 20–40 °C), 2% $N_2$, <1% $H_2$ with traces of $H_2S$, $O_2$, $NH_3$, halides and siloxanes [12,13]. The high levels of $CO_2$ and $CH_4$ enable the conversion of biogas to syngas (CO and $H_2$) by methane dry reforming (DR) reaction [14–16]:

$$CH_4 + CO_2 \rightarrow 2H_2 + 2CO \quad \Delta H_{298K}^0 = +247\ \text{kJ·mol}^{-1} \tag{1}$$
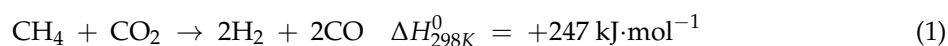
The high operating temperatures needed to perform the endothermic DR reaction lead to active species sintering and coke formation [17]. Besides, DR is accompanied by several side reactions, among which the methane cracking reaction ($CH_4 \rightarrow C + 2H_2$, $\Delta H_{298K}^0 = +75\ \text{kJ·mol}^{-1}$) and the Boudouard reaction ($2CO \rightarrow C + CO_2$, $\Delta H_{298K}^0 = -173\ \text{kJ·mol}^{-1}$) appear to be the most important [17,18]. The steam reforming (SR) of biogas is a combination of DR (Equation (1)) and methane SR (Equation (2)). The presence of steam reduces carbon formation by coke reforming reaction ($C + H_2O \rightarrow CO + H_2$, $\Delta H_{298K}^0 = +131\ \text{kJ·mol}^{-1}$) and increases $H_2$ concentration in the product mixture by favouring the water gas shift (WGS) reaction ($CO + H_2O \rightarrow CO_2 + H_2$, $\Delta H_{298K}^0 = -41\ \text{kJ·mol}^{-1}$) [19].

$$CH_4 + H_2O \rightarrow 3H_2 + CO \quad \Delta H_{298K}^0 = +206\ \text{kJ·mol}^{-1} \tag{2}$$

Moreover, in the oxy-steam reforming (OSR) of biogas, the presence of oxygen improves the energy efficiency of the process by exothermic methane partial/total oxidation reactions (Equations (3) and (4)), as well as favours coke oxidation ($C + O_2 \rightarrow CO_2$, $\Delta H_{298K}^0 = -394\ \text{kJ·mol}^{-1}$) [20,21].

$$CH_4 + O_2 \rightarrow 2H_2 + CO \quad \Delta H_{298K}^0 = -36\ \text{kJ·mol}^{-1} \tag{3}$$

$$CH_4 + 2O_2 \rightarrow 2H_2O + CO_2 \quad \Delta H_{298K}^0 = -802\ \text{kJ·mol}^{-1} \tag{4}$$

Biogas can be effectively transformed to syngas by reforming processes, with the aim to further upgrade it into bio-hydrogen, bio-fuels or chemicals. SR is a well-established conventional process for syngas production at industrial scale, which is usually carried out over Ni- and Ru-based pellet catalysts in tubular reactors [22,23], with severe heat and mass transport limitations [24]. As a toolbox of PI, structured catalysts provide a promising way to overcome these limitations thanks to enhanced heat and mass transfer coefficients, higher surface-to-volume ratio and lower pressure drop [25,26]. These characteristics enhance the catalytic performance of reforming reactions, allowing operation at high space velocity simultaneously reducing the amount of catalytic material [27,28]. Thus, the research interest in structured catalysts development is constantly growing [4,27,29–36].

Monolith-based catalysts have been tested successfully for reforming reactions with improved catalytic performance but limitations still exist due to the absence of radial mass and convective heat transfer in straight channels. On the other hand, the tortuous structure of ceramic open-cell foam (OCF) provides a fast radial heat and mass transport with higher contact efficiency [37,38]. Indeed, OCFs are macroporous reticulated three-dimensional (3D) structures in which the cells are connected by open windows, providing high porosity with 80–90% void space [39]. As an alternative

to conventional systems (pellets made of magnesium aluminate or calcium aluminate spinels), alumina OCFs are potential structured supports for reforming processes with proven mechanical, chemical and hydrothermal suitability for severe working conditions: high temperature (600–900 °C), high pressure (20–30 bar) and steam rich environment (S/CH$_4$ = 1.5–3.0) [40,41]. However, the catalytic functionalization of the foam structures still remains one of the main critical issues. In fact, the catalytic coated layer needs to be highly active and stable, as well as resistant to thermal and mechanical stresses occurring during reforming reactions [4,29,42]. The conventional washcoating technique suffers from non-uniformity and exfoliation of coatings, as well as binder contamination. Moreover, a proper use of the washcoating method implies the optimization of many parameters, such as pH, viscosity of the slurry, primers' and binders' utilization, speed of dipping and so forth. [7,30,43]. Recently, we proved that solution combustion synthesis (SCS) is a suitable procedure to in-situ deposit uniform, thin and high-strength catalytic layers on the surface of both ceramic monoliths [7,25,30–32] and foams [7,44]. The SCS method takes the advantage of an exothermic, very quick and self-sustaining chemical reaction between metal precursors and an organic fuel (i.e., urea), resulting in the synthesis of nanocrystalline oxide powders over the surface of structured supports [4,45–47].

In this paper, alumina OCFs with different pore density (20, 30 and 40 pore per square inch, ppi) were coated with Rh/CeO$_2$ catalyst by SCS. The coated structures were physically characterized by scanning electron microscopy with energy dispersive X-ray spectroscopy (SEM/EDX) and transmission electron microscopy (TEM) to analyse their morphological characteristics. The mechanical stability of the coating was analysed using ultrasound tests. The permeability and form coefficients were derived from pressure drop data. The catalytic performance was investigated towards biogas SR and OSR reactions, evaluating the effects of temperature and space velocity. Characteristics time analysis and dimensionless numbers were calculated to identify the reaction controlling regime. Stability tests were also performed as a function of time-on-stream (TOS).

## 2. Results

### 2.1. Characterization of Samples

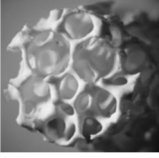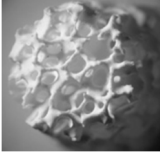#### 2.1.1. Geometrical Properties of OCFs Structures

Figure 1 shows one of the three structures used in this work (30 ppi OCF), with the characteristic geometric parameters and pore diameter distribution. OCFs are composed of cell units which are repeated in all space dimensions; cells are the void part enclosed by struts and interconnected pores (Figure 1a). The measured hole area (*A*) and strut thickness (*t$_s$*) (Figure 1b) were averaged among at least 250 images of 15 different bare supports. Pore diameter ($d_p = \sqrt{\frac{4A}{\pi}}$) was calculated by considering the hole as an equivalent circle [48]. A broad pore diameter distribution ranging from 1.0 to 2.0 mm was evaluated, as shown in Figure 1c.
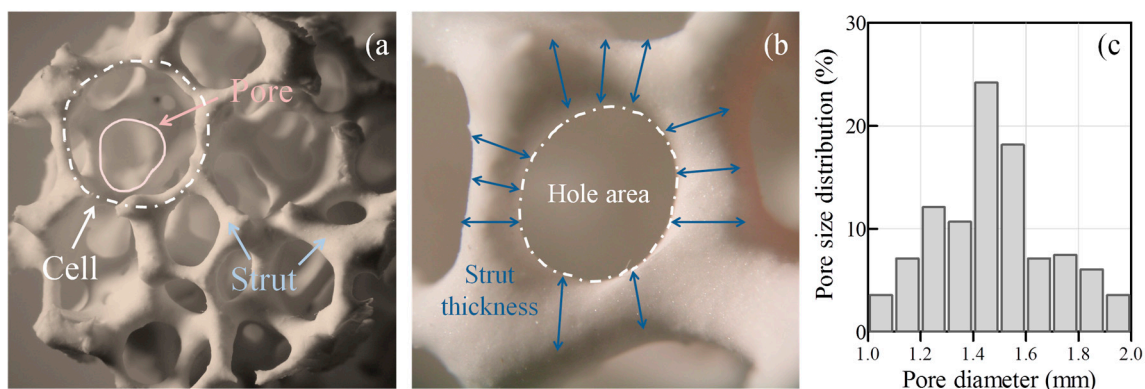


**Figure 1.** Geometric parameters (**a**,**b**) and pore diameter distribution (**c**) of 30 ppi alumina OCF structure.

Table 1 lists the geometrical properties of OCFs structures (20, 30 and 40 ppi) and the related equations. The voidage ($\varepsilon$) was calculated from the relative density ($\rho_r$) by the equation $\varepsilon = 1 - \left[ 2.59 \left( \frac{t_s}{t_s + d_p} \right)^2 \right]$ [49]. Bed porosity ($V_p$) was determined by helium pycnometry. The geometric surface area ($GSA$) was calculated according to the tetrakaidecahedron model reported by of Buciuman and Kraushaar-Czarnetzki [50].

**Table 1.** Geometrical characteristics of the investigated open cell foam (OCF) structures.

| Structured Substrate | F20 | F30 | F40 |
|---|---|---|---|
| Pore per inch, *ppi* | 20 | 30 | 40 |
| Diameter, $\phi$—Length, $L$ (mm) | 10–15 | 10–15 | 10–15 |
| Hole area, $A$ (mm$^2$) | 2.88 | 1.55 | 0.92 |
| Average pore diameter, $d_p$ (mm) $d_p = \sqrt{\frac{4A}{\pi}}$ | 1.92 | 1.40 | 1.08 |
| Average strut thickness, $t_s$ (mm) | 0.51 | 0.41 | 0.33 |
| Face diameter, $d_f$ (mm) $d_f = d_p + t_s$ | 2.42 | 1.81 | 1.41 |
| Relative density, $\rho_r$ $\rho_r = 2.59 \left( \frac{t_s}{d_f} \right)^2$ | 0.11 | 0.13 | 0.14 |
| Voidage, $\varepsilon$ $\varepsilon = 1 - \rho_r$ | 0.89 | 0.87 | 0.86 |
| Bed porosity, $V_p$ (%) | 88.3 | 85.1 | 83.6 |
| Geometric surface area, $GSA$ (m$^2 \cdot$m$^{-3}$) $GSA = \frac{4.82}{d_f} \cdot \sqrt{\rho_r}$ | 669 | 967 | 1273 |
| Exposed surface area, $SA_{OCF}$ (mm$^2$) $SA_{OCF} = V_{OCF} \cdot GSA$ | 788 | 1138 | 1500 |
| Catalyst loading, $C_{load}$ (mg$\cdot$cm$^{-2}$) $C_{load} = \frac{W_{cat}}{SA_{OCF}}$ | 22.2 | 15.2 | 12.0 |
| Catalytic layer thickness, $\delta_c$ (µm) | 25–40 | 15–30 | 5–20 |

### 2.1.2. Pressure Drop Measurements

Figure 2 shows the pressure drops of all OCFs structures measured at different superficial velocities, together with the theoretical estimations. As reported by several Authors [51–53], Forchheimer-extended Darcy equation is a valid model for describing the pressure drop in OCFs at fluid velocity higher than 0.1 m·s$^{-1}$. In the proposed model, the pressure drop per unit length ($\Delta P/L$) is expressed as a quadratic function of the inlet gas velocity ($u$) by the following equation:

$$\frac{\Delta P}{L} = au + bu^2 \tag{5}$$
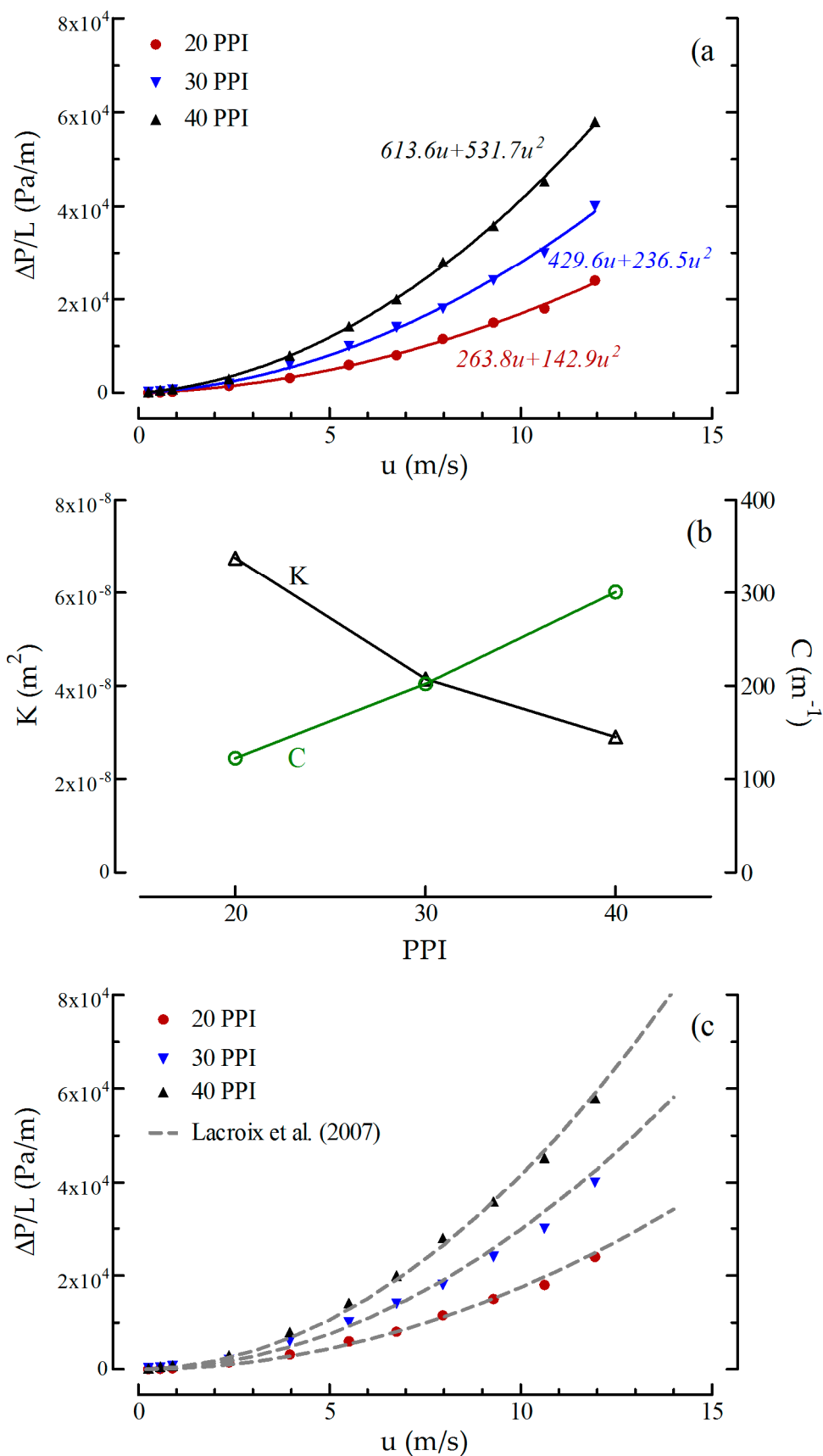
**Figure 2.** Pressure drop measurements for different foam density: Forchheimer-extended Darcy theoretical estimation (**a**); effect of pore density on the permeability and form coefficient (**b**); Lacroix-extended Ergun theoretical estimation (**c**).

The terms a and b represent the viscous drag and the inertial drag, respectively [48,54,55]. The first term ($a = \mu/K$) represents the linear dependence of pressure drop on flow velocity. It can be expressed as the ratio between the dynamic viscosity of the fluid ($\mu$) and the permeability of the foam ($K$). The second term ($b = \rho \cdot C$), representing the quadratic dependence of the pressure drop on flow velocity, can be determined from the product of fluid density ($\rho$) and the form coefficient of the foam ($C$) [53,54,56].

By fitting the measured pressure drop values as a quadratic function of the fluid velocity (Figure 2a), the two hydraulic properties of a porous medium, permeability ($K$) and form coefficient ($C$), were determined from a and b constants of the curve-fit, known the dynamic viscosity ($\mu_{N_2}$) = $1.78 \times 10^{-5}$ Pa·s) and density ($\rho_{N_2}$) = 1.17 kg·m$^{-3}$) of $N_2$. Indeed, the permeability decreased by increasing the pore density from $6.7 \times 10^{-8}$ (20 ppi OCF) to $2.9 \times 10^{-8}$ m$^2$ (40 ppi OCF). An opposite trend was observed for the form coefficient, which increased from 122.1 to 300.6 m$^{-1}$ for 20 ppi and 40 ppi OCFs, respectively (Figure 2b). Similar results were reported by Wang and Guo [54], measuring the pressure drop of different foams as a function of the material porosity.

In the literature, several researchers adopted Ergun model to explain and fit the experimental data [57–59]:

$$\frac{\Delta P}{L} = E_1 \frac{\mu_{N_2}(1-\varepsilon)^2}{\varepsilon^3 d_p^2} u + E_2 \frac{\rho_{N_2}(1-\varepsilon)}{\varepsilon^3 d_p} u^2 \tag{6}$$

where the Ergun constants $E_1$ and $E_2$, depending on the nature of the porous media, ranged between 100 to 865 and 0.65 to 2.65, respectively [59]. In the work of Lacroix et al. [60], a simple analogy between the traditional spherical particle bed and the foam was proposed. Thus, the values of 150 and 1.75 for $E_1$ and $E_2$, respectively, were used for the estimation of the pressure drop in OCFs with different porosity. As shown in Figure 2c, the Ergun model is in good agreement with our experimental data. As expected, the measured pressure drop increased by decreasing the pore diameter and voidage (Table 1), following the order F20 < F30 < F40 structures.

### 2.1.3. SEM/EDX Measurements

A homogeneous catalytic coating fully covering the OCFs was observed, without clogging of cells or pores (as highlighted in Figure 3a,b,d,e,g,h). The EDX mapping of the coated structured samples evidenced that ceria is well deposited on the alumina surface. Furthermore, rhodium seemed to be in turn well dispersed on the surface of ceria (Figure 3c,f,i). A homogeneous morphology of the catalytic layer was further evidenced in the cross-section view of the F40 system, highlighting a good interconnection between the foam and coated layer (Figure 4). Moreover, the catalyst particles penetrated into the porosity of the alumina foam, thus ensuring an optimal adhesion of the catalytic layer [61]. Indeed, a reduction of the macro-porosity of the alumina surface was observed after depositing the catalytic layer (see Figure S1 in Supplementary Materials).

In order to compare the catalytic behaviour of OCFs with different pore density, the same amount of catalyst (1.5 wt.% Rh immobilized over ~170 mg of ceria carrier) was deposited on each foam. The catalyst loading decreased from 22.2 to 12.0 mg·cm$^{-2}$ due to the increase of *GSA* from 669 (F20) to 1273 m$^2$·m$^{-3}$ (F40), as reported in Table 1. The higher the *GSA*, the thinner catalytic coated layer. Therefore, thickness values between 5–20 μm, 15–30 μm and 25–40 μm were determined for F40, F30 and F20 structures, respectively (Figure 5).
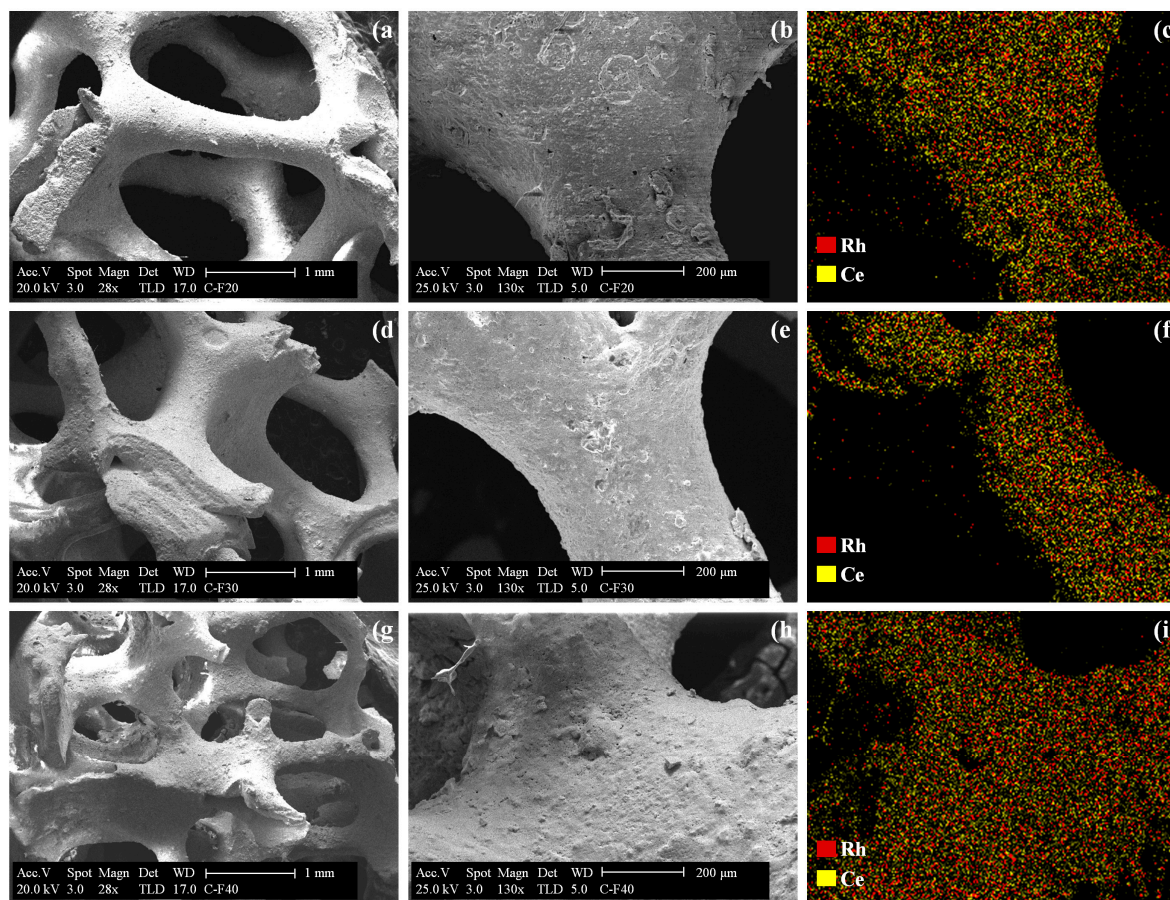
**Figure 3.** Scanning electron microscopy (SEM) micrographs at different magnification of the Rh/CeO$_2$-coated F20 (**a**,**b**), F30 (**d**,**e**) and F40 (**g**,**h**) structures and corresponding EDX mapping (**c**,**f**,**i**).
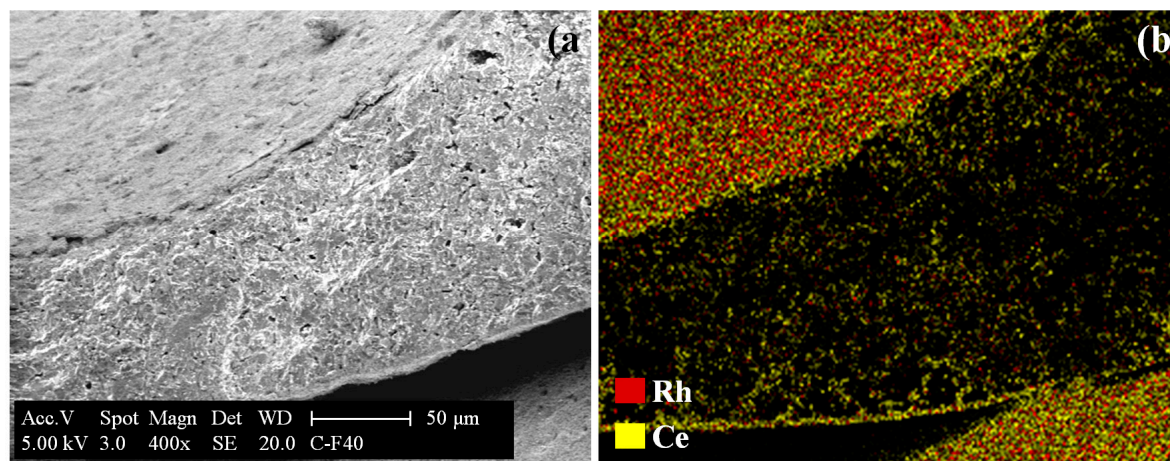


**Figure 4.** SEM micrographs of the Rh/CeO$_2$-coated F40 catalyst: cross section (**a**) and relative EDX mapping (**b**).
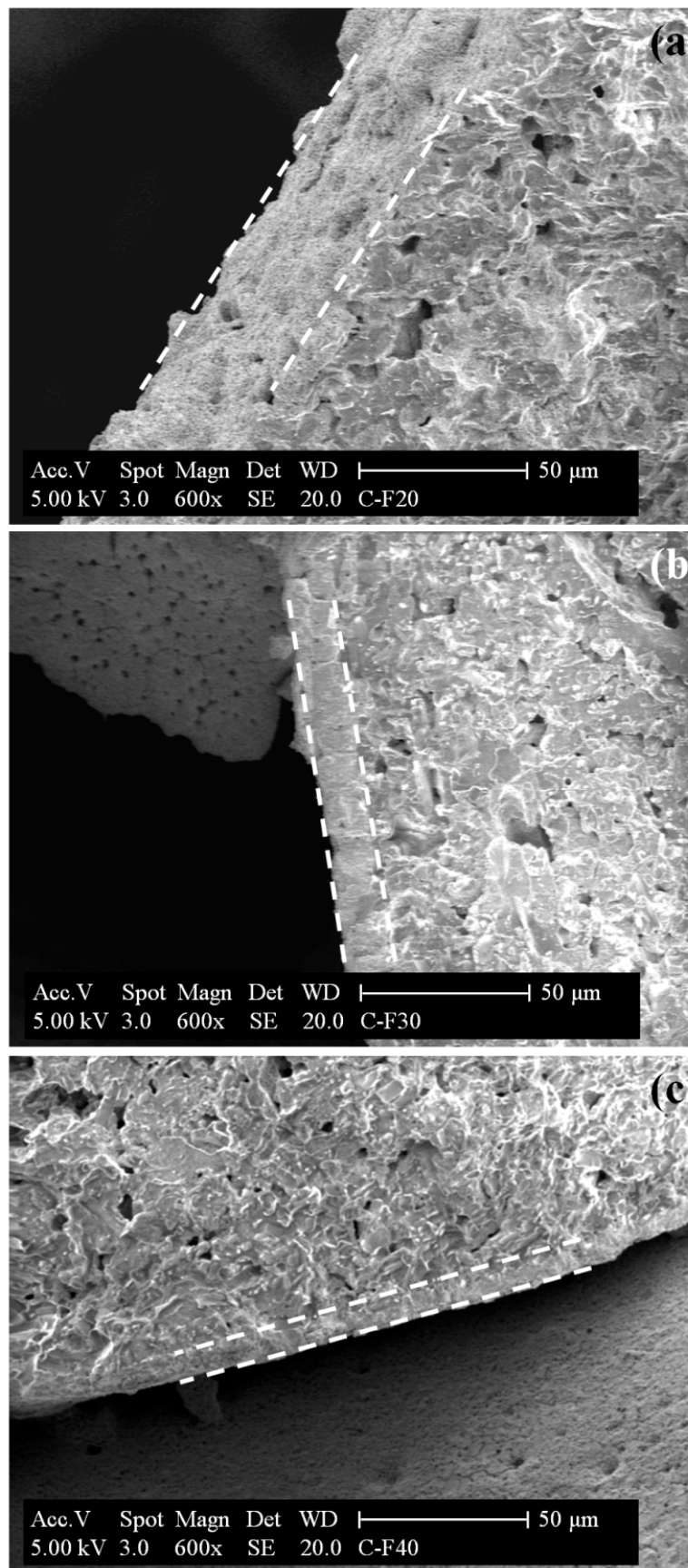
**Figure 5.** SEM images of 20 ppi (**a**), 30 ppi (**b**) and 40 ppi (**c**) coated layers.

### 2.1.4. Adhesion Measurements

The mechanical resistance of the coated layers onto the foam structures was evaluated by ultrasonic treatment in isopropyl alcohol solution. Figure 6 shows the weight loss of the coated F20, F30 and F40 structures after each stability cycle. In all cases, the adherence of the catalytic layer to the alumina support was very good, with weight losses lower than 5%, in agreement with the literature [7,30–32,44]. Therefore, SCS allowed overcoming the exfoliation of coatings usually encountered in conventional dip-coating techniques [7,39,62]. The good resistance of the coated layer to mechanical stress can be ascribed to the irregular porous surface of the support, which is beneficial to anchoring or interlocking the catalytic precursors (see Figure S1 in Supplementary Materials) [63]. The worst (but even good) stability was observed for the F20 OCF, probably due to the thicker catalyst layer compared to that of F30 and F40 structures (Figure 5). Similar results were previously reported by other Authors, suggesting that the pore density of the substrate influenced the adherence properties of the resulting systems [64,65]. An increase in pore density led to a decreased *GSA* and, in turn, increased thickness of the catalytic layer, hindering the adhesion of the coating due to the convex surface of the foam structures [65].
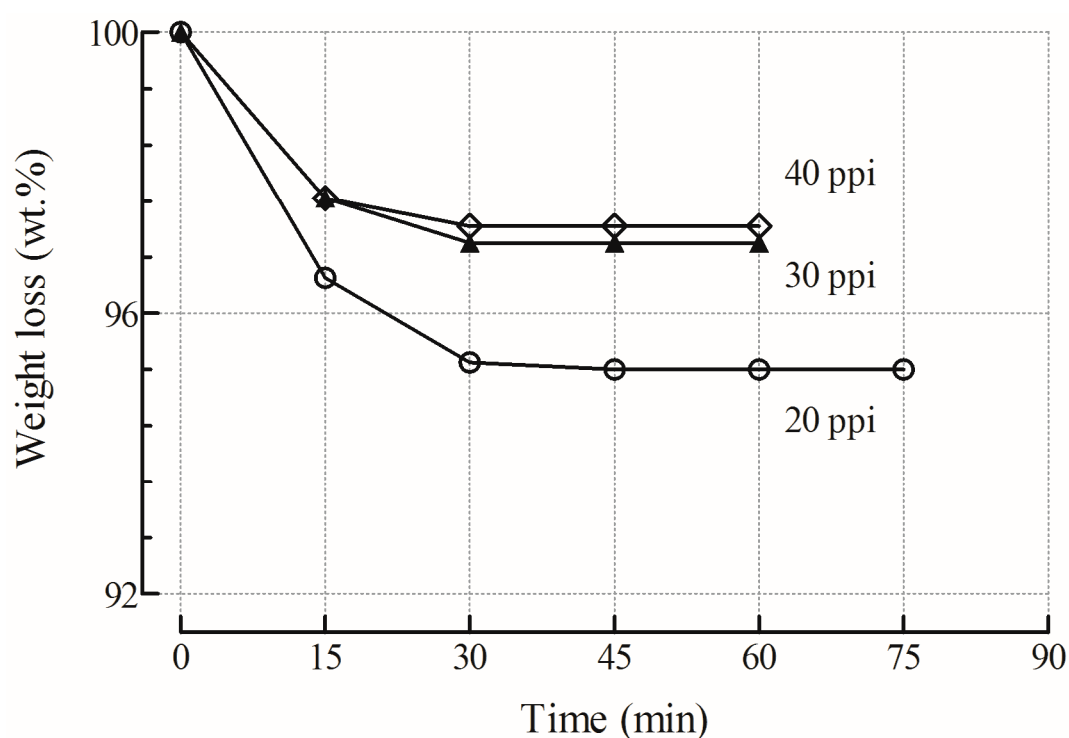


**Figure 6.** Weight loss as a function of time during the ultrasonic treatment of the coated foams.

### 2.1.5. TEM Measurements

The morphology of the $Rh/CeO_2$ catalytic layer was investigated by TEM analysis on the powder mechanically scraped from F40 alumina walls. TEM image in Figure 7 showed 40–70 nm $CeO_2$ particles in agglomerate form, with well distributed Rh particles, ranging between 2 and 7 nm. A similar morphology was previously observed for $Rh/CeO_2$ catalytic phase deposited on the inner walls of cordierite monoliths [30].
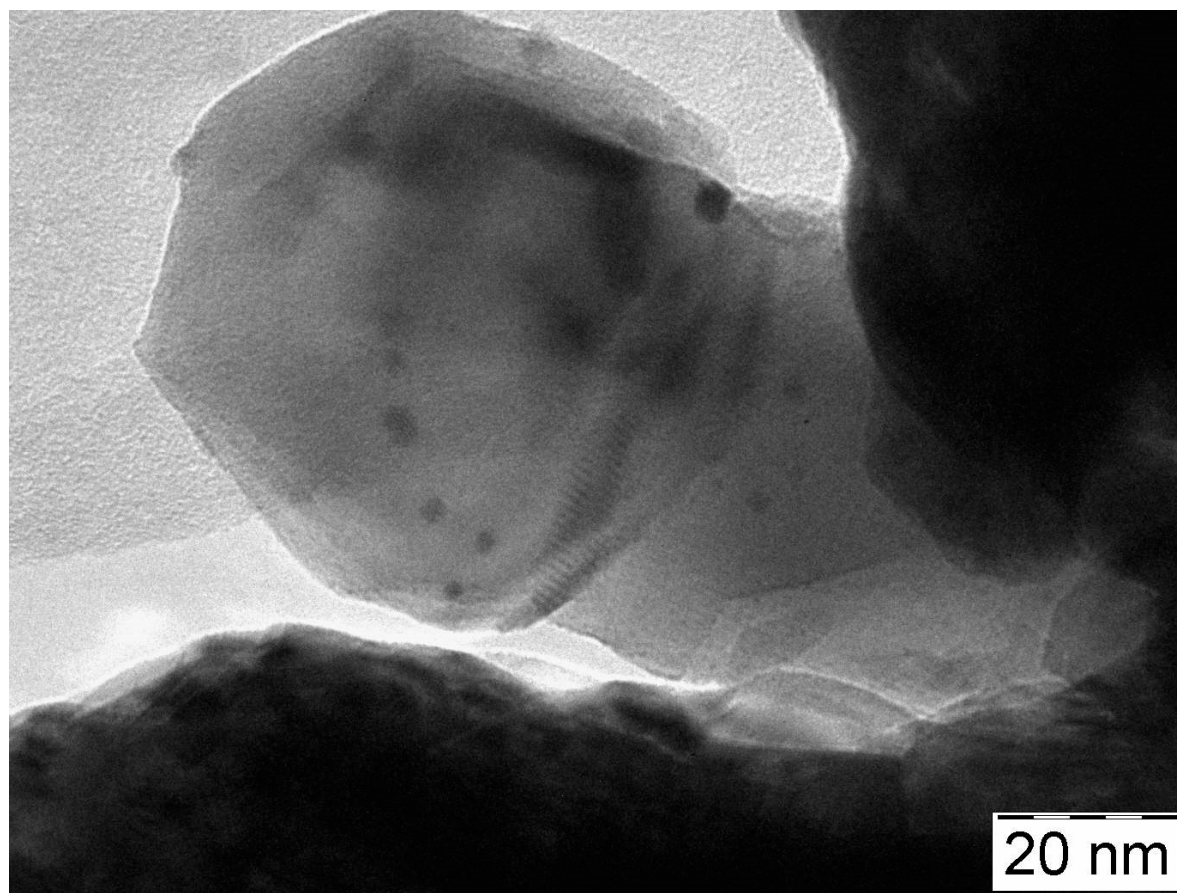
**Figure 7.** TEM images of the $Rh/CeO_2$ catalyst reduced at 300 $^\circ$C under hydrogen flow and scraped from the foam walls.

## 2.2. Catalytic Tests towards Biogas Steam and Oxy-Steam Reforming

### 2.2.1. Evaluation of External Interphase (Gas-Solid) and Internal Heat Transfer Limitations

Due to the consumption of reactants and the production or consumption of heat, temperature profiles can develop around the catalytic coating and inside the catalyst particles [66]. The criterion proposed by Mears [67] was used to check the significance of external interphase (gas-solid) heat transport limitations:

$$\frac{E_a \left(-\Delta H_r^0\right) R_{CH_4}}{h \, GSA \, R \, T_b^2} < 0.15 \tag{7}$$

Tee values calculated ranged between 0.037–0.133 (F20), 0.022–0.079 (F30) and 0.013–0.050 (F40). Indeed, the criterion was satisfied and therefore interphase heat transport limitations can be ignored. However, it could be noticed that the gas-solid heat transfer resistance increased by the decreasing of *GSA*, following the order F20 > F30 > F40.

The temperature gradients inside the catalytic coating can be neglected since the Anderson criterion (Equation (8)) was satisfied [67,68]:

$$\frac{E_a \left(-\Delta H_r^0\right) r_{CH_4} \, \rho_c \, \delta_c^2}{\lambda_c \, R \, T^2} < 0.75 \tag{8}$$

The values calculated (0.0001–000067) were found to be much lower than 0.75, mainly due to the extremely thin coating layer, as evidenced in SEM images (Figures 4 and 5). A detailed explanation of the Mears and Anderson criteria is provided in the Supplementary Materials.

### 2.2.2. Evaluation of External and Internal Mass Transfer Limitations

The tortuous nature of the OCFs structures allows high contact efficiency between reactants and catalyst. However, mass transfer limitations can still occur with strong impact on the catalytic performance [69]. The catalytic reaction between reactant molecules and active sites, generally located inside the catalyst pores, takes place after the reactant molecules diffuse from gas phase to the catalyst surface (external diffusion) and through the pores of the coated layer (internal diffusion). Thus, three operating regimes, namely kinetic, external mass transfer and internal diffusion, can control the reforming processes. In addition, it is important to exclude any type of mass transfer limitation in order to improve the mixing and optimize the geometry of the reforming reactor [69,70].

As previously reported [31], the characteristic time analysis is widely used to investigate physical and chemical processes involved in structured catalysts. A detailed explanation of the calculations is provided in the Supplementary Materials. To describe the trade-off between reaction kinetic (reaction time scale) and convective transport flux (diffusion time scale) the first Damkohler (*Da-I*) number was introduced as the ratio between the residence time ($t_c$) and the characteristic reaction time ($t_r$):

$$Da - I = \frac{t_c}{t_r} > 1 \tag{9}$$

The *Da-I* numbers calculated (2.8–3.2) were found to be greater than 1 due to high voidage of alumina OCFs (0.86–0.89, as shown in Table 1), confirming that the reactant mixture had sufficient time to react over the catalyst within OCFs pores. High *Da-I* values showed the potential to increase space velocity even at values higher than 140,000 $NmL \cdot g^{-1} \cdot h^{-1}$. This condition is necessary to ensure high reforming performances of the catalysts under investigation, while the influence of the external and internal mass transfer limitations was investigated by calculating the second Damköhler (*Da-II*) and the third Damköhler (*Da-III*) numbers, respectively [42,71–73].

The dimensionless *Da-II* number relates the reaction rate to the external transport phenomena in the system. It can be calculated from a relation between the characteristic external mass transfer time ($t_{ext}$) and the characteristic reaction time ($t_r$):

$$Da - II = \frac{t_{ext}}{t_r} < 0.1 \tag{10}$$

If *Da-II* number is greater than 0.1, external mass transfer limitations become important in the system, allowing for a concentration gradient between the bulk gas and the outside surface of the coated layer [74,75]. Figures 8a and 9a show the calculated values for biogas SR and OSR experiments, respectively. In both cases, *Da-II* increased by increasing the space velocity or by decreasing the pore density, whereas it was not much affected by the temperature [75]. Moreover, *Da-II* number lower than 0.1 (0.02–0.08) revealed the absence of external diffusion limitations at all the investigated conditions. However, F20 catalyst showed *Da-II* numbers close to 0.1 (0.08) at 140,000 $NmL \cdot g^{-1} \cdot h^{-1}$, indicating that the reactants could not have enough time for mass transfer and reaction. The effect of external diffusion on the reforming activity was also estimated by the Carberry criterion for a first-order reaction with respect to methane [76,77]:

$$Ca = \frac{R_{CH_4}}{k_G \ GSA \ C_{CH_4}} < 0.05 \tag{11}$$
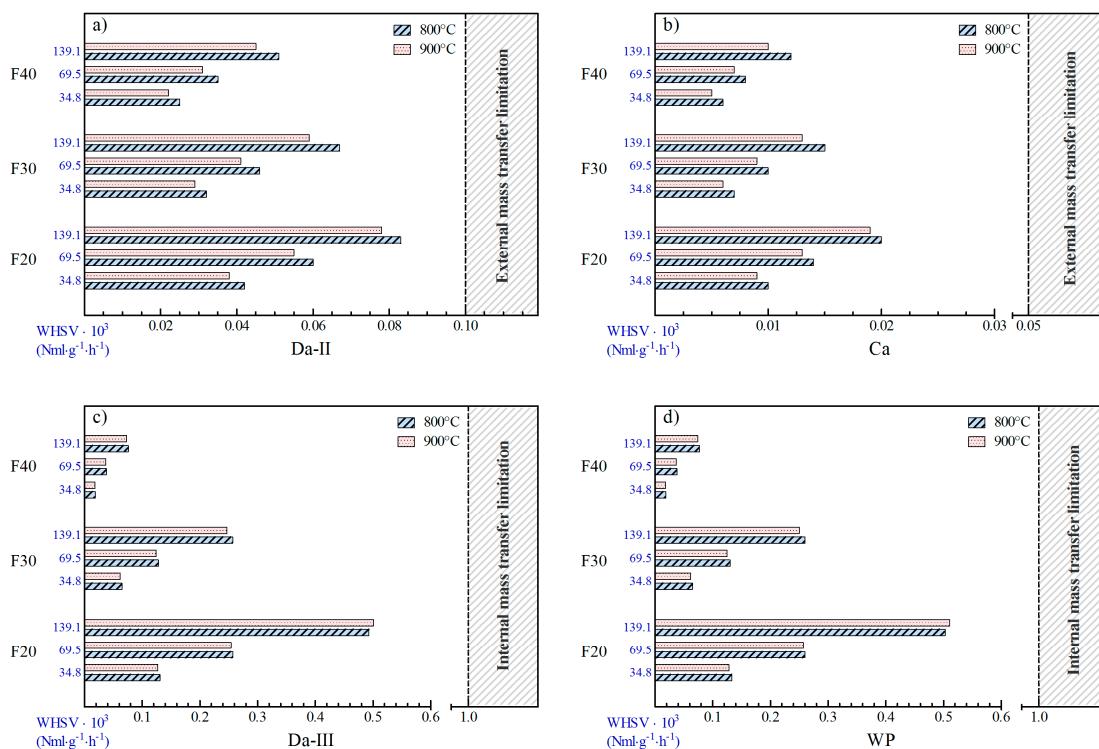
**Figure 8.** Influence of temperature and space velocity on (**a**) *Da-II*, (**b**) *Ca*, (**c**) *Da-III* and (**d**) *WP* dimensionless numbers on biogas SR experiments over F20, F30 and F40 catalysts.
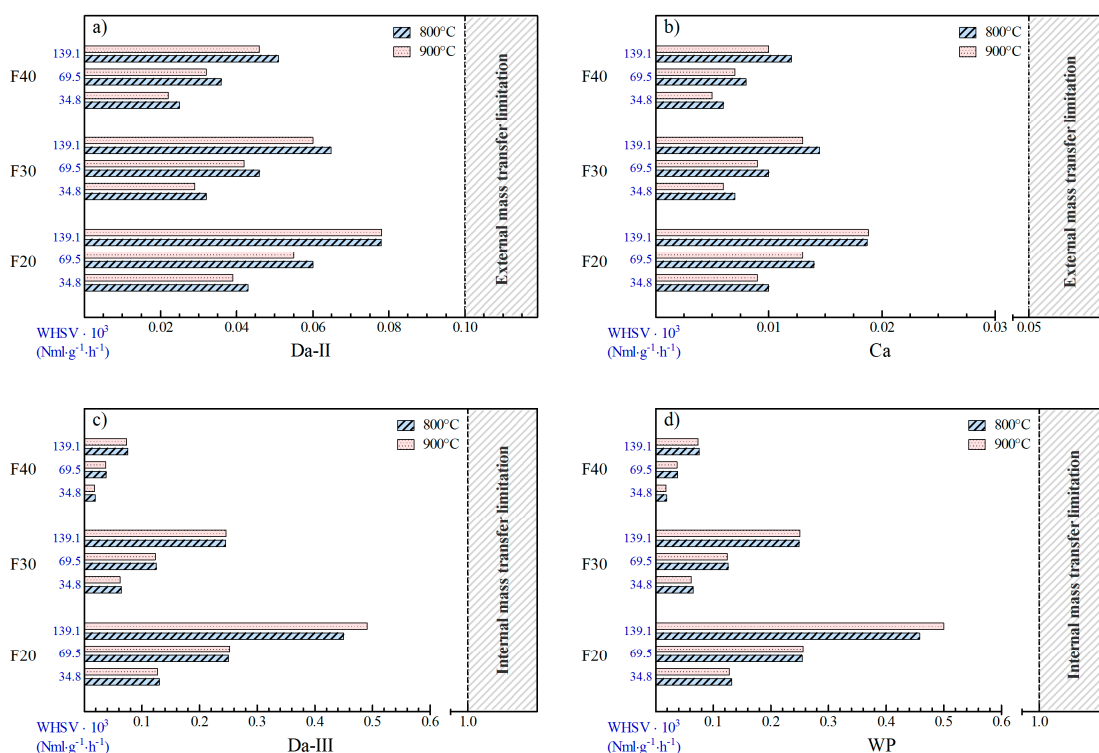


**Figure 9.** Influence of temperature and space velocity on (**a**) *Da-II*, (**b**) *Ca*, (**c**) *Da-III* and (**d**) *WP* dimensionless numbers on biogas OSR experiments over F20, F30 and F40 catalysts.

According to *Ca* numbers, the results showed that biogas SR (Figure 8b) and OSR (Figure 9b) experiments were not affected by external diffusion limitations, confirming the results obtained by

calculating *Da-II*. However, high pore density OCF (F40) with smaller pore diameter and higher geometric surface area (Table 1) emerged as the more adequate configuration.

The internal mass transfer limitations were investigated by calculating the third Damköhler number (*Da-III*) as the ratio between the characteristic coated layer diffusion time ($t_{int}$) and the characteristic reaction time ($t_r$):

$$Da - III = \frac{t_{int}}{t_r} < 1 \tag{12}$$

*Da-III* values (0.02–0.50) lower than 1 excluded any internal mass transfer controlling regime at all the investigated conditions (Figures 8c and 9c). Thus, reactants rapidly diffused through the pores of the coated layer, avoiding the formation of concentration gradients between the catalyst surface and active sites [78,79]. These results were also confirmed by using the Weisz-Prater criterion [25,31], as reported in Figure 8d (biogas SR) and Figure 9d (biogas OSR).

$$WP = \frac{r_{CH_4}\, \rho_c\, \delta_c{}^2}{D_{CH_4,e}\, C_{CH_4,s}} < 1 \tag{13}$$

The *WP* values calculated (0.02–0.50) highlighted the absence of any internal mass transfer limitation, mainly due to thin coating thickness provided by the SCS method (Figure 5).

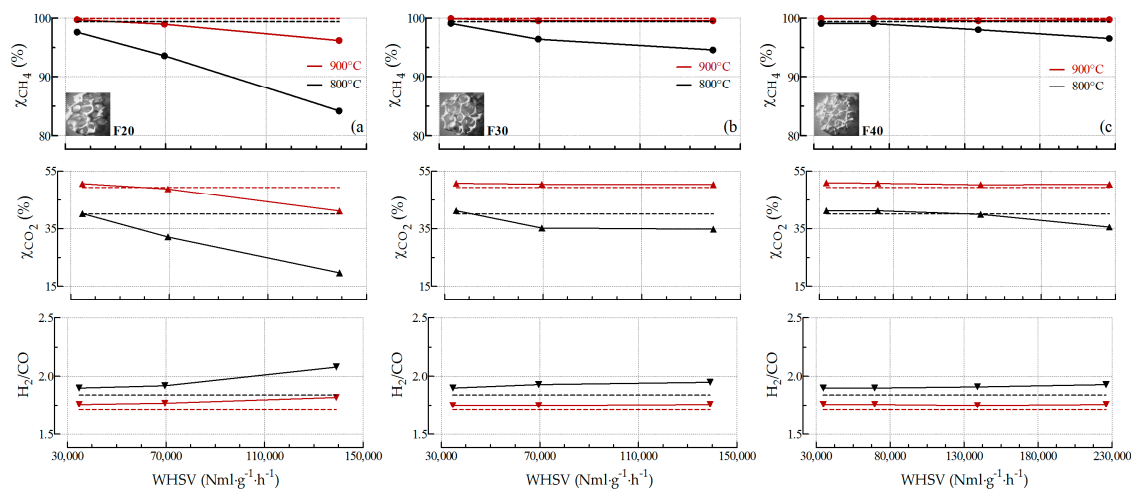### 2.2.3. Influence of the Pore Density on Biogas SR and OSR Activity

Figure 10 shows the influence of temperature ($T_{SET}$ = 800–900 °C) and space velocity (WHSV = 35,000–140,000 NmL·g$^{-1}$·h$^{-1}$) on biogas SR activity in terms of $CH_4$ and $CO_2$ conversion and $H_2$/CO molar ratio. Thermodynamic data are also reported for comparison. The F20 structured catalyst showed almost total $CH_4$ conversion at 900 °C and 35,000 NmL·g$^{-1}$·h$^{-1}$ (Figure 10a), slightly decreasing afterwards to ca. 98% by increasing the space velocity up to 140,000 NmL·g$^{-1}$·h$^{-1}$. The same trend was observed for $CO_2$ conversion, which decreased from 16 to 10%, remaining slightly higher than the equilibrium value, due to the effect of the reverse WGS reaction [30,32,33]. This result led to $H_2$/CO ratios (2.60–2.73) slightly lower than the thermodynamic values (2.74). Both $CH_4$ and $CO_2$ conversions decreased by decreasing the temperature and increasing the space velocity (Figure 10a). Indeed, the F20 sample showed ca. 98% of $CH_4$ conversion at 800 °C and 35,000 NmL·g$^{-1}$·h$^{-1}$, which lowered to ca. 92% at 140,000 NmL·g$^{-1}$·h$^{-1}$, due to the decreased contact time between reactants and catalyst. Moreover, negative values of $CO_2$ conversion were revealed as the result of the competition between DR (Equation (1)), SR (Equation (2)) and WGS reactions [19,33,80]. Indeed, at high steam content (S/$CH_4$ = 3), $CH_4$ reacted preferentially with steam due to the more stable nature of $CO_2$, leading to a lower contribution of the DR reaction. Simultaneously, the greater contribution of the $CO_2$-producing WGS reaction led to a negative $CO_2$ conversion at 800 °C and 140,000 NmL·g$^{-1}$·h$^{-1}$ (Figure 10a). Similar trends were reported by Ashrafi et al. [81]; $CO_2$ conversion data ranged from ca. −27% to 10% were shown at S/$CH_4$ ratio of 2.71 in the temperature range of 600–900 °C [81]. The decrease in catalytic activity by increasing the space velocity was less pronounced as the pore density increased to 30 ppi (Figure 10b, F30) and 40 ppi (Figure 10c, F40). In fact, F30 and F40 catalysts showed almost total (<99%) and stable $CH_4$ conversion at all the investigated conditions.

Similarly, the pore density of OFCs affected the OSR activity. Figure 11 shows the influence of temperature ($T_{SET}$ = 800–900 °C) and space velocity (WHSV = 35,000–140,000 NmL·g$^{-1}$·h$^{-1}$) on biogas OSR activity for the three OCFs catalysts, along with the thermodynamic data, reported as dotted lines. At WHSV of 35,000 NmL·g$^{-1}$·h$^{-1}$, the experimental results were very close to the equilibrium calculations for all the structured catalysts. However, both $CH_4$ and $CO_2$ conversion decreased by increasing space velocity over the F20 system (Figure 11a), leading to an increase of the $H_2$/CO ratio [82,83]. As expected, a higher activity was observed by increasing the pore density to 30 and 40 ppi. At high temperature (900 °C), the F30 and F40 catalysts showed $CH_4$ (99.6%) and $CO_2$ (50.6%) conversion very close to the equilibrium at all the investigated space velocities. Instead, a slight

decrease of $CH_4$ conversion from ca. 99 to 95% was observed at 800 °C by increasing the space velocity up to 140,000 $NmL \cdot g^{-1} \cdot h^{-1}$ over the F30 system (Figure 11b). In these conditions, the F40 catalyst still showed high $CH_4$ conversion (ca. 98–99%), which slightly decreased to ca. 96% by further increasing the space velocity up to 140,000 $NmL \cdot g^{-1} \cdot h^{-1}$.
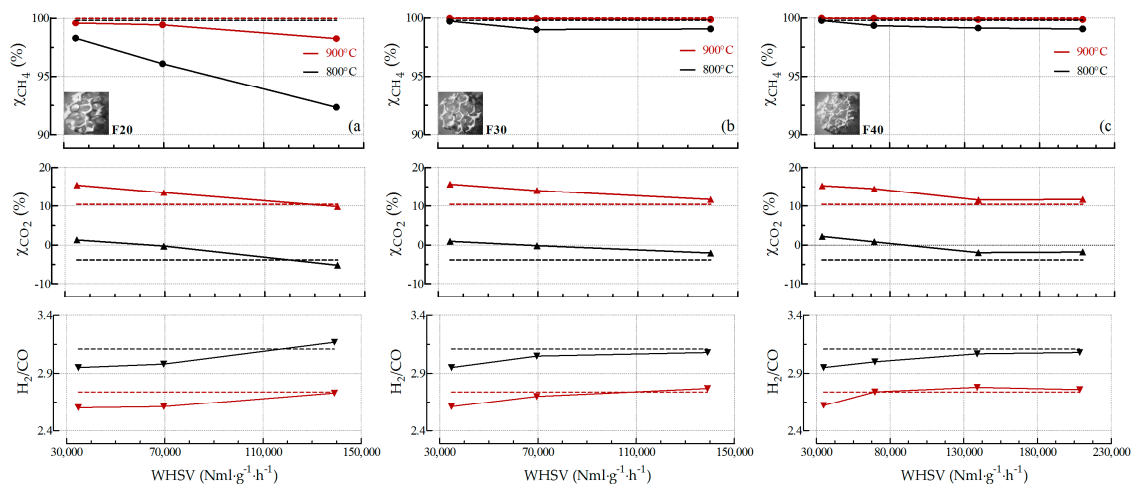


**Figure 10.** Biogas SR activity (S/$CH_4$ = 3) over F20 (**a**), F30 (**b**) and F40 (**c**) catalysts. Influence of temperature ($T_{SET}$ = 800–900 °C) and space velocity (WHSV = 35,000–140,000 $NmL \cdot g^{-1} \cdot h^{-1}$) on $CH_4$ conversion and $H_2$/CO molar ratio (thermodynamic data reported as dotted lines).



**Figure 11.** Biogas OSR activity (S/$CH_4$ = 1; $O_2$/$CH_4$ = 0.2) over F20 (**a**), F30 (**b**) and F40 (**c**) catalysts. Influence of temperature ($T_{SET}$ = 800–900 °C) and space velocity (WHSV = 35,000–140,000 $NmL \cdot g^{-1} \cdot h^{-1}$) on $CH_4$ conversion, $CO_2$ conversion and $H_2$/CO molar ratio (thermodynamic data reported as dotted lines).

### 2.2.4. Stability towards SR and OSR Processes

The stability evaluation is a noticeable issue in commercial application of heterogeneous structured catalysts [33,84]. Long-term tests were carried out over F40 catalyst at extreme operative conditions, such as $T_{SET}$ = 900 °C and GHSV = 70,000 $NmL \cdot g^{-1} \cdot h^{-1}$, with consecutive start-up and shut-down cycles. Figure 12 shows the results as $CH_4$ and $CO_2$ conversion and effluent composition over 200 h TOS for both SR (Figure 12a) and OSR (Figure 12b) experiments. Clearly, the F40 catalyst showed a steady performance, with negligible changes during the stability tests, indicating that the Rh/$CeO_2$ catalytic phase did not deactivate during TOS. Only a slight deactivation was observed for biogas SR

test after 150 h, probably due to a slight sintering of Rh active phase induced by the high reaction temperature, as previously reported [30].
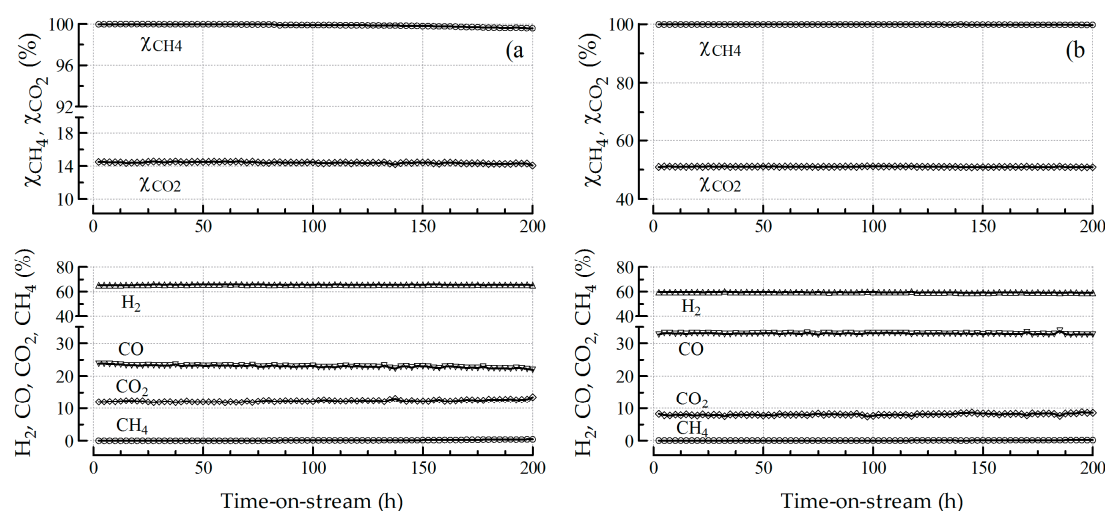


**Figure 12.** Biogas SR (**a**) and OSR (**b**) stability over F40 catalyst. $CH_4$ conversion, $CO_2$ conversion and effluent composition as a function of time-on-stream ($T_{SET}$ = 900 °C; WHSV = 70,000 NmL·g$^{-1}$·h$^{-1}$).

## 3. Discussion

The SR and OSR activity of OCFs coated with Rh/CeO$_2$ catalyst increased with pore density of the structures under investigation (Figures 10 and 11). As the number of catalyst active sites were fixed per unit volume of alumina foam by using the same catalyst loading (1.5 wt.% Rh immobilized over ~170 mg of ceria carrier), the observed catalytic performances indicated the importance of catalyst layer thickness and geometric characteristics. Indeed, activity results could be attributed first to the exposed surface area of the catalysts. In fact, the increase of *GSA* from 669 (F20) to 1273 m$^2$·m$^{-3}$ (F40) (Table 1) led to an increase in both SR and OSR activity following the order F20 < F30 ≈ F40. Moreover, a decrease in pore diameter resulted in improved heat and mass transport properties, as evidenced by the results of the previously discussed criteria.

Although the Mears criterion revealed the absence of external interphase (gas-solid) heat transport limitations, as well as Damköhler (*Da-II*) and Carberry numbers revealed the absence of external mass transfer limitations, the observed transport properties can play an important role in determining the catalytic performances. The values of these criteria decreased with increasing pore density, which indicated the enhancement in heat and mass transfer characteristics. It is well known that the fluid turbulence caused by tortuous flow path and radial convective flows is a major cause of gas-solid heat transfer improvement. Therefore, the increase in pressure drop values with pore density (Figure 3) led to higher turbulence and improved transport characteristics with potential reduction of reactor size. The higher values on the F20 catalyst estimated by Mears criterion were indicative of lower gas-solid heat transfer efficiency, contributing to the lower catalytic activity of F20 catalyst as compared to F30 and F40 systems. Similarly, the high external mass transfer resistance (Figures 8 and 9) of F20 catalyst allowed for a concentration gradient between the bulk gas and catalyst surface, leading to a drop in reactants conversion (Figures 10a and 11a) while almost stable activity was observed for F30 and F40 catalysts, due to their improved transport properties, as confirmed by *Da-II* and Carberry numbers. Mbodji et al. [85] reported comparable results on methane SR in a millistructured reactor. In their study, external mass transfer limitations appeared on a highly active catalyst at high temperature and large hydraulic diameter (< 1 mm). Arzamendi et al. [86] showed that in the case of Rh-based catalyst, it was needed to decrease the hydraulic diameter below 0.4 mm to eliminate external mass transfer limitations for process intensification. In addition, the lower porosity and pores size of the 40 ppi

system led to higher pressure drop (Figure 2) and increased residence time of reactants, thus resulting as the more adequate configuration for hydrogen production [87].

As reported by several Authors [88–91], the thickness of the coated layer strongly affects both the heat and reactants diffusion through the catalyst pores. Indeed, the resistance to internal diffusion increased with increasing the coating thickness, leading to higher Anderson criterion values (heat transfer limitations), as well as higher *Da-III* and W-P numbers (mass transfer limitations) [31,38,69,79]. In this regard, a thicker catalyst layer (such as > 100–150 μm) still remains a major issue of the systems prepared by conventional washcoating technique [62,92,93]. If the washcoat is thin and well anchored, all the active sites are accessible to reagents but the amount of catalyst could be not sufficient to process the inflowing reactants, decreasing $CH_4$ and $CO_2$ conversions. On the other side, the greater the amount of catalyst, the thicker washcoated layer, resulting in internal transfer limitations. Thus, high reactor throughput requires an excellent control of the catalyst layer thickness, that need to be sufficient (to ensure high $H_2$ yield) and sufficiently thin (to guarantee the absence of internal limitation) [91,94], as demonstrated also for other catalytic reactions [95]. As most interesting conclusion, the SCS method allowed the in-situ deposition of very thin (5–40 μm) catalytic layers (Table 1), avoiding internal heat and mass transfer limitations and positively affecting the performance towards biogas reforming processes. Moreover, this resulted in increased volumetric catalyst productivity for high reactor throughput with increasing in pore density while operating in kinetic control regime.

## 4. Experimental Section

### 4.1. Chemicals and Foams

Technical grade cerium nitrate ($Ce(NO_3)_3 \cdot 3H_2O$), rhodium nitrate ($Rh(NO_3)_3 \cdot nH_2O$), urea ($CH_4N_2O$), isopropyl alcohol ($C_3H_8O$) and acetone ($C_3H_6O$) were purchased from Sigma-Aldrich (St. Louis, MO, USA). All aqueous solutions were prepared using ultrapure water (Millipore Milli-Q system with resistivity > 18 MΩ cm). High purity (99.999 vol%) $CH_4$, $CO_2$, $H_2$, $N_2$ and $O_2$ gases were supplied in cylinders by Rivoira S.p.A. (Milan, Italy). Alumina-based ceramic OCFs with pore density of 20, 30 and 40 ppi were purchased from Lanik S.r.o. (Czech Republic).

### 4.2. Catalysts Preparation

Cylindrical OCFs (10 mm diameter, 15 mm length) were sonicated in water/acetone (50/50 vol.%) mixture for 30 min and dried at 120 °C for 2 h. The structured catalysts were prepared in two subsequent steps: (i) SCS procedure to in-situ deposit the $CeO_2$ carrier and (ii) WI of the Rh active phase.

Briefly, the OCFs were dipped in an aqueous solution containing cerium nitrate as precursor and urea as fuel, then introduced into a muffle furnace preheated at 600 °C for ca. 10 min to initiate the combustion reaction and rapidly cooled down to room temperature in few minutes. The process was repeated for 4–6 times to deposit ca. 170 mg of $CeO_2$ carrier [25,30,32,46,47]. Figure 13 shows the loaded $CeO_2$ carrier versus the number of immersion cycles for different substrates. 4 cycles were needed for 40 ppi OCF due to its relatively high *GSA* (Table 1), while 6 cycles were required to deposit approximately the same $CeO_2$ loading (170 mg) on 20 ppi OCF.

Then, the 1.5 wt.% Rh active phase was deposited by WI technique. The coated structures were dipped in an aqueous solution of rhodium precursor, calculated based on the deposited $CeO_2$ carrier. After each immersion, the structures were dried at 120 °C for ca. 10 min. Afterwards, the coated OCFs were calcined at 800 °C in static air for 2 h.

The analysis of the diffraction pattern of coated OCF showed the characteristic peaks of both cubic $CeO_2$ fluorite and $\alpha$-$Al_2O_3$ phase, while no diffraction peaks of Rh oxides were detected, due to the low loading and high dispersion of the noble metal (see Figure S2 in Supplementary Materials) [96–99].

The calculated catalyst loading, as amount of $Rh/CeO_2$ catalyst per exposed surface area of the foam structure, followed the order 40 ppi OCF ($12.0 \text{ mg} \cdot \text{cm}^{-2}$) < 30 ppi OCF ($15.2 \text{ mg} \cdot \text{cm}^{-2}$) < 20 ppi OCF ($22.2 \text{ mg} \cdot \text{cm}^{-2}$) (Table 1).
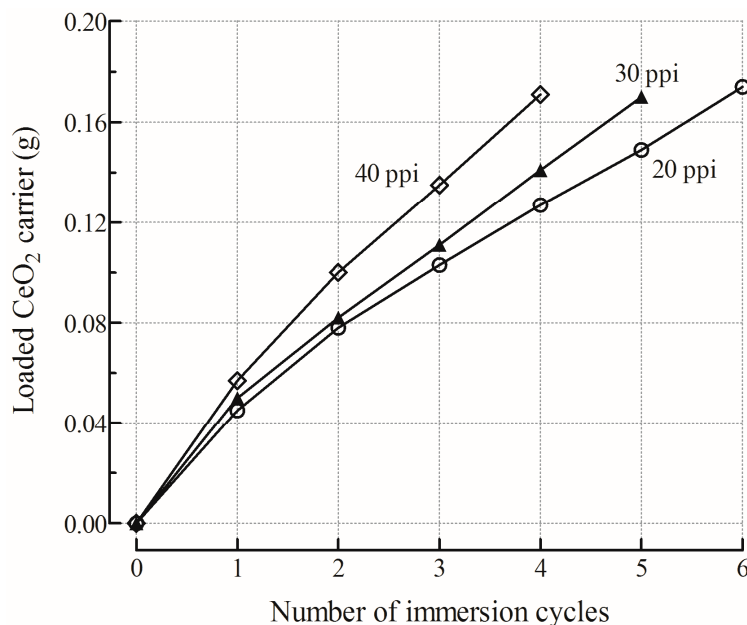
**Figure 13.** Evolution of the loaded CeO$_2$ carrier after sequential immersion cycles of the different OCFs.

### 4.3. Physicochemical Characterization

All OCFs were scanned with Nikon SMZ1500 Stereoscope (Nikon Cooperation, Tokyo, Japan) and the images processed by ImageJ software (NIH, Bethesda, MD, USA) to measure characteristic geometric dimensions.

OCFs porosity was determined by helium pycnometry using a Micromeritics 1305 Multivolume Pycnometer (Norcross, GA, USA).

X-ray diffraction (XRD) patterns were recorded by a Philips X-Pert 3710 diffractometer (Almelo, the Netherlands) with a scanning speed of $1.50°·min^{-1}$ over the range $2\theta = 20°–75°$. The diffractometer was equipped with a Cu K$\alpha$ radiation source, operating at 40 kV and 20 mA. The coated OCF was finely ground before the measurements. The peaks were assigned according to the PCPFWIN database. The CeO$_2$ crystallite size was calculated by the Scherrer equation based on the CeO$_2$ (111) reflection peak.

N$_2$ adsorption-desorption was carried out at liquid nitrogen temperature (196 °C) with a Micromeritics ASAP 2020 instrument (Micrometrics Inc., Norcross, GA, USA) to measure the Brunauer-Emmett-Teller (BET) specific surface area Barrett-Joyner-Halenda (BJH) pore volume. The samples were degassed by heating at 300 °C under vacuum for 6 h before the measurement.

A U-tube manometer connected to the reactor containing the OCFs was used to measure the pressure drop at different superficial velocities. N$_2$ flow was supplied at ambient temperature by a mass flow-meter (Brooks Instrument, Hatfield, PA, USA) and measured by a digital flow-meter (Agilent ADM 2000, Santa Clara, CA, USA). The height difference between the two columns of water in the two branches of the U-tube manometer was converted into pressure drop via the Stevin's law $\left( \Delta z = \frac{\Delta P}{g·\rho_{H_2O}} \right)$ [7].

The coating procedure was evaluated in terms of homogeneity of the coating, amount of catalyst deposited and adhesion force. SEM/EDX images were collected by using a Philips XL-30 FEG ESEM (FEI-Phillips, Hillsboro, OR, USA) in order to analyse the morphological characteristics of the coatings deposited onto the structures. The structured samples were cut longitudinally to evaluate the thickness of the catalytic layer. At least 30 images for each OCF were collected. The adherence of the coating layer was evaluated in terms of weight loss after ultrasonic treatment in 50 vol.% isopropyl alcohol solution. The coated OCFs were treated for 15 min at 45 kHz and 130 W using the USC 900D ultrasonic

bath and dried for 1 h at 120 °C. The sequence was repeated several times until the weight loss stayed stable. The weight loss percentage was referred to the catalytic layer deposited.

TEM micrographs were obtained using a Philips CM12 instrument (FEI-Phillips, Hillsboro, OR, USA). The reduced coating layer was scraped from the OCF walls, dispersed in isopropyl alcohol by ultrasonic treatment and placed on holey copper grids.

### 4.4. Catalytic Tests

A detailed description of the experimental setup is provided in our previous publications [25,30,32,46,47]. Biogas SR and OSR experiments were carried out at atmospheric pressure in a quartz fixed-bed reactor. The structured catalysts were placed at the centre of the reactor and inserted into a furnace equipped with a PID temperature controller. A simulated biogas ($CH_4$:$CO_2$ = 60:40 *v/v*) was used for the investigations. SR experiments were carried out at fixed steam-to-methane molar ratio (S/$CH_4$ = 3), varying temperature ($T_{SET}$ = 800–900 °C) and space velocity (WHSV = 35,000–140,000 $NmL \cdot g^{-1} \cdot h^{-1}$, defined as hourly volume of the gaseous feed per gram of catalytic layer). Similarly, OSR experiments were carried out at fixed S/$CH_4$ = 1 and oxygen-to-methane molar ratio ($O_2$/$CH_4$ = 0.2). Activity tests were conducted for 6 h and repeated three times to verify the repeatability. Catalyst stability was investigated over 200 h of TOS through consecutive start-up and shut-down cycles as accelerated stress test. Before the catalytic tests, the structured catalysts were reduced in-situ with a flow of $H_2$/$N_2$ (50/50 vol.%, 30 $Nml \cdot min^{-1}$) at 300 °C for 1 h. Mass flow controllers (Brooks Instrument Smart Mass Flow, Hatfield, PA, USA) were used to measure and control the flow of gaseous reactants. Steam was fed using an isocratic pump (Agilent 1100 Series) and an evaporator. The composition of reagents and products was determined using an on-line gas chromatograph (Agilent 6890 Plus) equipped with thermal conductivity (TCD) and flame ionization (FID) detectors. The results are reported in terms of $CH_4$ conversion ($\chi_{CH_4}$), $CO_2$ conversion ($\chi_{CO_2}$) and hydrogen-to-carbon monoxide ratio ($H_2$/CO) in reaction products. Chemical composition in thermochemical equilibrium was calculated with HSC Chemistry 7.1$^{®}$ calculation software (Outotec Oyj Technologies, Espoo, Finland), using the Gibbs free-energy minimization method.

## 5. Conclusions

As potential structured catalytic supports, alumina open-cell foams (OCFs) with different pore density (20, 30 and 40 ppi) were investigated towards biogas steam reforming (SR) and oxidative steam reforming (OSR) processes for syngas production. Catalytic alumina OCFs were synthesized with a thin and uniform Rh/$CeO_2$ catalyst layer by coupling: (i) solution combustion synthesis (SCS) to in-situ deposit the $CeO_2$ carrier and (ii) wet impregnation (WI) of the Rh active phase. Various physico-chemical characterization techniques were utilized to determine geometric and catalytic characteristics of bare and coated foams. Then, the catalytic performance of coated foams was evaluated at atmospheric pressure by varying temperature (800–900 °C) and space velocity (35,000–140,000 $NmL \cdot g^{-1} \cdot h^{-1}$). Characteristic time analysis and dimensionless numbers were calculated to assess the prevalence of the kinetic regime on mass and heat transfer limitations. OCFs showed a variation in pore size with increasing pore density which further influenced the other geometric and catalytic characteristics. The results of characterization techniques (XRD, SEM/EDX and TEM) highlighted the non-dependence of physico-chemical characteristics of coated catalysts on the geometry of the OCFs, with the exception of the catalyst layer thickness. Ultrasound adherence tests confirmed the excellent mechanical resistance of the coated layers, with weight losses lower than 5%. The structured catalysts showed outstanding results in biogas SR and OSR, following the activity order 20 ppi < 30 ppi ≈ 40 ppi, mainly due to the increased geometric surface area, heat and mass transfer properties. No internal and external heat and mass transport limitations were observed as evaluated by different criteria. A very homogeneous and thin (ranging from 5 to 40 μm with increasing the pore density) catalytic coated layer was successfully deposited by using the SCS technique which resulted in negligible internal heat

and mass transport limitations and excellent catalytic performance. The decrease in pore size of the alumina OCF resulted in higher pressure drop and fluid turbulence, leading to improved gas-solid transport characteristics and catalytic performances with potential reduction of reactor size. A stable catalytic activity of F40 structured catalyst was observed over 200 h of TOS for both biogas SR and OSR processes.

**Supplementary Materials:** The following are available online at http://www.mdpi.com/2073-4344/8/10/448/s1, Figure S1. SEM micrographs of bare (a,c,e) and $Rh/CeO_2$-coated (b,d,f) OCFs: F20 (a,b), F30 (c,d) and F40 (e,f) structures (inset: images of the macroscopic bare OFCs), Figure S2. XRD pattern of $Rh/CeO_2$ as a powder, bare and $Rh/CeO_2$-coated F30 (included also reference peaks of $CeO_2$: JPDS 4-593 and reference peaks of $Al_2O_3$: JPDS 10-0173).

**Author Contributions:** All Authors have written the manuscript. C.I. has prepared the samples and performed the catalytic tests. C.I. and A.V. performed XRD, BET and SEM analysis. M.A.A. and S.S. determined geometric properties and pressure drops. M.A.A., C.I. and C.W.M.Q. performed the calculations. A.V., L.P. and S.S. coordinated the research activities.

**Conflicts of Interest:** The authors declare no conflict of interest.

## Nomenclature

| | | |
|---|---|---|
| ***OCFs properties*** | $d_p$ | Average pore diameter (m) |
| | $d_f$ | Average face diameter (m) |
| | $GSA$ | Geometric surface area ($m^2 \cdot m^{-3}$) |
| | $L$ | Length (m) |
| | $OFA$ | Open frontal area ($m^2$) |
| | $\varepsilon$ | Voidage |
| | $\phi$ | Diameter (m) |
| ***Coated layer properties*** | $d_{p,c}$ | Average coated pore diameter (m) |
| | $d_{f,c}$ | Average coated face diameter (m) |
| | $r_p$ | Pore radius (m) |
| | $\delta_c$ | Coated layer thickness (m) |
| | $\varepsilon_c$ | Coated layer porosity |
| | $\lambda_c$ | Coated layer effective thermal conductivity ($kW \cdot m^{-1} \cdot K^{-1}$) |
| | $\rho_c$ | Coated layer density ($kg \cdot m^{-3}$) |
| | $\tau$ | Tortuosity factor |
| ***Reaction data*** | $E_a$ | Apparent activation energy ($J \cdot mol^{-1}$) |
| | $F_{tot}$ | Total gas flow rate ($m^3 \cdot s^{-1}$) |
| | $P$ | Reaction pressure (kPa) |
| | $T$ | Reaction temperature (K) |
| | $T_b$ | Bulk fluid temperature (K) |
| | $T_{IN}$ | Inlet bed temperature (K) |
| | $T_{OUT}$ | Outlet bed temperature (K) |
| | $r_{CH_4}$ | Reaction rate for $CH_4$ ($kmol \cdot kg^{-1} \cdot s^{-1}$) |
| | $R_{CH_4}$ | Volumetric reaction rate for $CH_4$ ($kmol \cdot m^{-3} \cdot s^{-1}$) |
| | $\Delta H_r^0$ | Standard reaction enthalpy ($J \cdot mol^{-1}$) |

| | | |
|---|---|---|
| ***Dimensionless Numbers*** | $Ca$ | Carberry number |
| | $E_1$ | Ergun Constant |
| | $E_2$ | Ergun Constant |
| | $Nu$ | Nusselt number |
| | $Re$ | Reynold number |
| | $Sc$ | Schmidt number |
| | $Sh$ | Sherwood number |
| | $WP$ | Weisz-Prater number |
| ***Fluid Properties*** | $C_{CH_4}$ | Methane concentration in feed mixture (kmol·m$^{-3}$) |
| | $C_{CH_4,s}$ | Methane concentration at catalyst surface (kmol·m$^{-3}$) |
| | $D_{CH_4}$ | Diffusivity of CH$_4$ in gas phase (m$^2$·s$^{-1}$) |
| | $D_{CH_4,e}$ | Effective diffusivity of CH$_4$ in coated layer (m$^2$·s$^{-1}$) |
| | $D_{CH_4-i}$ | Binary diffusion of CH$_4$ and $i$ gas species (m$^2$·s$^{-1}$) |
| | $D_k$ | Knudsen diffusion (m$^2$·s$^{-1}$) |
| | $h$ | Gas-solid heat transfer coefficient (kW·m$^{-2}$·K$^{-1}$) |
| | $k_G$ | Mass transfer coefficient of CH$_4$ (m·s$^{-1}$) |
| | $M_{CH_4}$ | Molecular weight of CH$_4$ (kg·kmol$^{-1}$) |
| | $M_i$ | Molecular weight of $i$ compound (kg·kmol$^{-1}$) |
| | $M_j$ | Molecular weight of $j$ compound (kg·kmol$^{-1}$) |
| | $M_{mix}$ | Molecular weight of gas mixture (kg·kmol$^{-1}$) |
| | $P_{c,i}$ | Critical pressure of $i$ compound (kPa) |
| | $R$ | Universal gas constant (J·mol$^{-1}$·K$^{-1}$) |
| | $T_{c,i}$ | Critical temperature of $i$ compound (K) |
| | $u$ | Inlet gas velocity (m·s$^{-1}$) |
| | $y_i$ | Mole fraction of $i$ compound |
| | $\lambda_i$ | Thermal conductivity of $i$ compound (kW·m$^{-1}$·K$^{-1}$) |
| | $\lambda_{mix}$ | Thermal conductivity of gas mixture (kW·m$^{-1}$·K$^{-1}$) |
| | $\mu_{H_2}$ | Viscosity of H$_2$ (kg·m$^{-1}$·s$^{-1}$) |
| | $\mu_{H_2O}$ | Viscosity of H$_2$O (kg·m$^{-1}$·s$^{-1}$) |
| | $\mu_i$ | Viscosity of $i$ compound (kg·m$^{-1}$·s$^{-1}$) |
| | $\mu_j$ | Viscosity of $j$ compound (kg·m$^{-1}$·s$^{-1}$) |
| | $\mu_{mix}$ | Viscosity of gas mixture (kg·m$^{-1}$·s$^{-1}$) |
| | $\mu_{N_2}$ | Viscosity of N$_2$ (kg·m$^{-1}$·s$^{-1}$) |
| | $\rho_{mix}$ | Density of gas mixture (kg·m$^{-3}$) |
| | $\rho_{N_2}$ | Density of N$_2$ (kg·m$^{-3}$) |
| | $v_{CH_4}$ | Molar volume of CH$_4$ (cm$^3$·mol$^{-1}$) |
| | $v_i$ | Molar volume of $i$ compound (cm$^3$·mol$^{-1}$) |
| ***Characteristic Times*** | $t_c$ | Characteristic contact time (s) |
| | $t_{ext}$ | Characteristic external mass transfer time (s) |
| | $t_{int}$ | Characteristic coated layer diffusion time (s) |
| | $t_r$ | Characteristic reaction time (s) |

## References

1. Lewandowski, I. *Bioeconomy. Shaping the Transition to a Sustainable, Biobased Economy*; Springer: Berlin, Germany, 2018; pp. 5–74. ISBN 978-3-319-68152-8.
2. Piemonte, V.; De Falco, M.; Basile, A. *Sustainable Development in Chemical Engineering: Innovative Technologies*; John Wiley & Sons Ltd.: Chichester, UK, 2013; pp. 95–118. ISBN 978-1-118-62984-0.
3. Balzarotti, R.; Ciurlia, M.; Cristiani, C.; Paparella, F. Washcoat deposition of Ni- and Co-ZrO$_2$ low surface area powders onto ceramic open-cell foams: Influence of slurry formulation and rheology. *Catalysts* **2015**, *5*, 2271–2286. [CrossRef]

4.  Specchia, S.; Ercolino, G.; Karimi, S.; Italiano, C.; Vita, A. Solution combustion synthesis for preparation of structured catalysts: A mini-review on process intensification for energy applications and pollution control. *J. Self-Propag. High-Temp. Synth.* **2017**, *26*, 166–186. [CrossRef]

5.  Moulin, J.A.; Stankewicz, A.; Kapteijn, F. The pontential of structured reactors in process intensification. *Chem. Sustainable Dev.* **2003**, *11*, 3–9.

6.  Williams, J.L. Monolith structures, materials, properties and uses. *Catal. Today* **2001**, *69*, 3–9. [CrossRef]

7.  Ercolino, G.; Karimi, S.; Stelmachowski, P.; Specchia, S. Catalytic combustion of residual methane on alumina monoliths and open cell foams coated with Pd/$Co_3O_4$. *Chem. Eng. J.* **2017**, *326*, 339–349. [CrossRef]

8.  Cybulski, A.; Moulijn, J.A. *Structured Catalysts and Reactors*, 2nd ed.; CRC Press, Taylor & Francis Group: Boca Raton, FL, USA, 2005; pp. 1–18. ISBN 978-1-4200-2800-3.

9.  Pfau, S.F.; Hagens, J.E.; Dankbaar, B. Biogas between renewable energy and bio-economy policies—Opportunities and constraints resulting from a dual role. *Energy. Sustain. Soc.* **2017**, *7*, 1–15. [CrossRef]

10.  Nahar, G.; Mote, D.; Dupont, V. Hydrogen production from reforming of biogas: Review of technological advances and an Indian perspective. *Renew. Sust. Energy Rev.* **2017**, *76*, 1032–1052. [CrossRef]

11.  Lo Faro, M.; Vita, A.; Pino, L.; Aricò, A.S. Performance evaluation of a solid oxide fuel cell coupled to an external biogas tri-reforming process. *Fuel Process. Technol.* **2013**, *115*, 238–245. [CrossRef]

12.  Farhad, S.; Yoo, Y.; Hamdullahpur, F. Effects of fuel processing methods on industrial scale biogas-fuelled solid oxide fuel cell system for operating in wastewater treatment plants. *J. Power Sources* **2010**, *195*, 1446–1453. [CrossRef]

13.  Rasi, S.; Veijanen, A.; Rintala, J. Trace compounds of biogas from different biogas production plants. *Energy* **2007**, *32*, 1375–1380. [CrossRef]

14.  Rathod, V.; Bhale, P.V. Experimental investigation on biogas reforming for syngas production over an alumina based nickel catalyst. *Energy Procedia* **2014**, *54*, 236–245. [CrossRef]

15.  Lino, A.V.P.; Assaf, E.M.; Assaf, J.M. Hydrotalcites derived catalysts for syngas production from biogas reforming: Effect of nickel and cerium load. *Catal. Today* **2017**, *289*, 78–88. [CrossRef]

16.  Eltejaei, H.; Reza Bozorgzadeh, H.; Towfighi, J.; Reza Omidkhah, M.; Rezaei, M.; Zanganeh, R.; Zamaniyan, A.; Zarrin Ghalam, A. Methane dry reforming on Ni/$Ce_{0.75}Zr_{0.25}O_2$–$MgAl_2O_4$ and Ni/$Ce_{0.75}Zr_{0.25}O_2$-$\gamma$–alumina: Effects of support composition and water addition. *Int. J. Hydrogen Energy* **2012**, *37*, 4107–4118. [CrossRef]

17.  Löfberg, A.; Kane, T.; Guerrero-Caballero, J.; Jalowiecki-Duhamel, L. Chemical looping dry reforming of methane: Toward shale-gas and biogas valorization. *Chem. Eng. Process. Process Intensif.* **2017**, *122*, 523–529. [CrossRef]

18.  Lahijani, P.; Zainal, Z.A.; Mohammadi, M.; Mohamed, A.R. Conversion of the greenhouse gas $CO_2$ to the fuel gas CO via the boudouard reaction: A review. *Renew. Sustain. Energy Rev.* **2015**, *41*, 615–632. [CrossRef]

19.  Vita, A.; Italiano, C.; Previtali, D.; Fabiano, C.; Palella, A.; Freni, F.; Bozzano, G.; Pino, L.; Manenti, F. Methanol synthesis from biogas: A thermodynamic analysis. *Renew. Energy* **2018**, *118*, 673–684. [CrossRef]

20.  Song, C.; Pan, W. Tri-reforming of methane: A novel concept for catalytic production of industrially useful synthesis gas with desired $H_2$/CO ratios. *Catal. Today* **2004**, *98*, 463–484. [CrossRef]

21.  Cipitì, F.; Pino, L.; Vita, A.; Laganà, M.; Recupero, V. Model-based investigation of a CO preferential oxidation reactor for polymer electrolyte fuel cell systems. *Int. J. Hydrogen Energy* **2007**, *32*, 4040–4051. [CrossRef]

22.  Holladay, J.D.; Hu, J.; King, D.L.; Wang, Y. An overview of hydrogen production technologies. *Catal. Today* **2009**, *139*, 244–260. [CrossRef]

23.  Joensen, F.; Rostrup-Nielsen, J.R. Conversion of hydrocarbons and alcohols for fuel cells. *J. Power Sources* **2002**, *105*, 195–201. [CrossRef]

24.  Karakaya, M.; Keskin, S.; Avci, A.K. Parametric study of methane steam reforming to syngas in a catalytic microchannel reactor. *Appl. Catal. A Gen.* **2012**, *411–412*, 114–122. [CrossRef]

25.  Vita, A.; Italiano, C.; Pino, L.; Frontera, P.; Ferraro, M.; Antonucci, V. Activity and stability of powder and monolith-coated Ni/GDC catalysts for $CO_2$ methanation. *Appl. Catal. B Environ.* **2018**, *226*, 384–395. [CrossRef]

26.  Frey, M.; Édouard, D.; Roger, A.-C. Optimization of structured cellular foam-based catalysts for low-temperature carbon dioxide methanation in a platelet milli-reactor. *C. R. Chim.* **2015**, *18*, 283–292. [CrossRef]

27. Ricca, A.; Palma, V.; Martino, M.; Meloni, E. Innovative catalyst design for methane steam reforming intensification. *Fuel* **2017**, *198*, 175–182. [CrossRef]

28. Tomašić, V.; Jović, F. State-of-the-art in the monolithic catalysts/reactors. *Appl. Catal. A gen.* **2006**, *311*, 112–121. [CrossRef]

29. Weng, J.; Lu, X.; Gao, P.-X. Nano-array integrated structured catalysts: A new paradigm upon conventional wash-coated monolithic catalysts? *Catalysts* **2017**, *7*, 253. [CrossRef]

30. Vita, A.; Cristiano, G.; Italiano, C.; Pino, L.; Specchia, S. Syngas production by methane oxy-steam reforming on Me/CeO$_2$ (Me = Rh, Pt, Ni) catalyst lined on cordierite monoliths. *Appl. Catal. B Environ.* **2015**, *162*, 551–563. [CrossRef]

31. Ashraf, M.A.; Sanz, O.; Italiano, C.; Vita, A.; Montes, M.; Specchia, S. Analysis of Ru/La-Al$_2$O$_3$ catalyst loading on alumina monoliths and controlling regimes in methane steam reforming. *Chem. Eng. J.* **2018**, *334*, 1792–1807. [CrossRef]

32. Vita, A.; Cristiano, G.; Italiano, C.; Specchia, S.; Cipitì, F.; Specchia, V. Methane oxy-steam reforming reaction: Performances of Ru/$\gamma$-Al$_2$O$_3$ catalysts loaded on structured cordierite monoliths. *Int. J. Hydrogen Energy* **2014**, *39*, 18592–18603. [CrossRef]

33. Roy, P.S.; Song, J.; Kim, K.; Kim, J.-M.; Park, C.S.; Raju, A.S.K. Effects of CeZrO$_2$–Al$_2$O$_3$ support composition of metal-foam-coated Pd–Rh catalysts for the steam-biogas reforming reaction. *J. Ind. Eng. Chem.* **2018**, *62*, 120–129. [CrossRef]

34. Zapf, R.; Thiele, R.; Wichert, M.; O'Connell, M.; Ziogas, A.; Kolb, G. Application of rhodium nanoparticles for steam reforming of propane in microchannels. *Catal. Commun.* **2013**, *41*, 140–145. [CrossRef]

35. Sadykov, V.; Mezentseva, N.; Fedorova, Y.; Lukashevich, A.; Pelipenko, V.; Kuzmin, V.; Simonov, M.; Ishchenko, A.; Vostrikov, Z.; Bobrova, L.; et al. Structured catalysts for steam/autothermal reforming of biofuels on heat-conducting substrates: Design and performance. *Catal. Today* **2015**, *251*, 19–27. [CrossRef]

36. Govender, S.; Friedrich, H.B. Monoliths: A review of the basics, preparation methods and their relevance to oxidation. *Catalysts* **2017**, *7*, 62. [CrossRef]

37. Carty, M.W.; Lednor, P.W. Monolithic ceramics and heterogeneous catalysts: Honeycombs and foams. *Curr. Opin. Solid State Mater. Sci.* **1996**, *1*, 88–95. [CrossRef]

38. Voltolina, S.; Marín, P.; Díez, F.V.; Ordóñez, S. Open-cell foams as beds in multiphase reactors: Residence time distribution and mass transfer. *Chem. Eng. J.* **2017**, *316*, 323–331. [CrossRef]

39. Zhao, G.; Liu, Y.; Lu, Y. Foam/fiber-structured catalysts: Non-dip-coating fabrication strategy and applications in heterogeneous catalysis. *Sci. Bull.* **2016**, *61*, 745–748. [CrossRef]

40. Faure, R.; Rossignol, F.; Chartier, T.; Bonhomme, C.; Maître, A.; Etchegoyen, G.; Del Gallo, P.; Gary, D. Alumina foam catalyst supports for industrial steam reforming processes. *J. Eur. Ceram. Soc.* **2011**, *31*, 303–312. [CrossRef]

41. Faure, R.; Basile, F.; Bersani, I.; Chartier, T.; Cuni, A.; Cornillac, M.; Gallo, P.D.; Etchegoyen, G.; Gary, D.; Rossignol, F.; et al. Foam-supported catalysts tailored for industrial steam reforming processes. In *Studies in Surface Science and Catalysis*; Gaigneaux, E.M., Devillers, M., Eds.; Elsevier: Amsterdam, The Netherlands, 2010; pp. 241–244. ISBN 978-0-444-53601-3.

42. Laguna, O.H.; Domínguez, M.I.; Centeno, M.A.; Odriozola, J.A. Catalysts on metallic surfaces: Monoliths and microreactors. In *New Materials for Catalytic Applications*; Parvulescu, V.I., Kemnitz, E., Eds.; Elsevier: Amsterdam, The Netherlands, 2016; pp. 81–120. ISBN 978-0-444-63587-7.

43. Balzarotti, R.; Italiano, C.; Pino, L.; Cristiani, C.; Vita, A. Ni/CeO$_2$-thin ceramic layer depositions on ceramic monoliths for syngas production by oxy steam reforming of biogas. *Fuel Process. Technol.* **2016**, *149*, 40–48. [CrossRef]

44. Ercolino, G.; Stelmachowski, P.; Specchia, S. Catalytic performance of Pd/Co$_3$O$_4$ on SiC and ZrO$_2$ open cell foams for process intensification of methane combustion in lean conditions. *Ind. Eng. Chem. Res.* **2017**, *56*, 6625–6636. [CrossRef]

45. Rivero-Mendoza, D.E.; Stanley, J.N.G.; Scott, J.; Aguey-Zinsou, K.-F. An alumina-supported Ni-La-based catalyst for producing synthetic natural gas. *Catalysts* **2016**, *6*, 170–184. [CrossRef]

46. Italiano, C.; Vita, A.; Fabiano, C.; Laganà, M.; Pino, L. Bio-hydrogen production by oxidative steam reforming of biogas over nanocrystalline Ni/CeO$_2$ catalysts. *Int. J. Hydrogen Energy* **2015**, *40*, 11823–11830. [CrossRef]

47.  Vita, A.; Italiano, C.; Fabiano, C.; Laganà, M.; Pino, L. Influence of Ce-precursor and fuel on structure and catalytic activity of combustion synthesized Ni/CeO$_2$ catalysts for biogas oxidative steam reforming. *Mater. Chem. Phys.* **2015**, *163*, 337–347. [CrossRef]

48.  Patcas, F.C.; Garrido, G.I.; Kraushaar-Czarnetzki, B. CO oxidation over structured carriers: A comparison of ceramic foams, honeycombs and beads. *Chem. Eng. Sci.* **2007**, *62*, 3984–3990. [CrossRef]

49.  Gibson, L.J.; Ashby, M.F. *Cellular Solids Structure and Properties*, 2nd ed.; Cambridge University Press: Cambridge, UK, 1999; pp. 15–51. ISBN 0521499119.

50.  Buciuman, F.C.; Kraushaar-Czarnetzki, B. Ceramic foam monoliths as catalyst carriers. 1. Adjustment and Description of the Morphology. *Ind. Eng. Chem. Res.* **2003**, *42*, 1863–1869. [CrossRef]

51.  Bhattacharya, A.; Calmidi, V.V.; Mahajan, R.L. Thermophysical properties of high porosity metal foams. *Int. J. Heat. Mass Transf.* **2002**, *45*, 1017–1031. [CrossRef]

52.  Boomsma, K.; Poulikakos, D.; Ventikos, Y. Simulations of flow through open cell metal foams using an idealized periodic cell structure. *Int. J. Heat Fluid Flow* **2003**, *24*, 825–834. [CrossRef]

53.  Hamadouche, A.; Nebbali, R.; Benahmed, H.; Kouidri, A.; Bousri, A. Experimental investigation of convective heat transfer in an open-cell aluminum foams. *Exp. Therm. Fluid Sci.* **2016**, *71*, 86–94. [CrossRef]

54.  Wang, H.; Guo, L. Experimental investigation on pressure drop and heat transfer in metal foam filled tubes under convective boundary condition. *Chem. Eng. Sci.* **2016**, *155*, 438–448. [CrossRef]

55.  Richardson, J.; Remue, D.; Hung, J.-K. Properties of ceramic foam catalyst supports: Mass and heat transfer. *Appl. Catal. A Gen.* **2003**, *250*, 319–329. [CrossRef]

56.  Richardson, J.; Peng, Y.; Remue, D. Properties of ceramic foam catalyst supports: Pressure drop. *Appl. Catal. A Gen.* **2000**, *204*, 19–32. [CrossRef]

57.  Nie, Z.; Lin, Y.; Tong, Q. Numerical investigation of pressure drop and heat transfer through open cell foams with 3D Laguerre-Voronoi model. *Int. J. Heat Mass Transfer* **2017**, *113*, 819–839. [CrossRef]

58.  Ergun, S.; Orning, A.A. Fluid flow through randomly packed columns and fluidized beds. *Ind. Eng. Chem.* **1949**, *41*, 1179–1184. [CrossRef]

59.  Edouard, D.; Lacroix, M.; Huu, C.P.; Luck, F. Pressure drop modeling on SOLID foam: State-of-the art correlation. *Chem. Eng. J.* **2008**, *144*, 299–311. [CrossRef]

60.  Lacroix, M.; Nguyen, P.; Schweich, D.; Huu, C.P.; Savin-Poncet, S.; Edouard, D. Pressure drop measurements and modeling on SiC foams. *Chem. Eng. Sci.* **2007**, *62*, 3259–3267. [CrossRef]

61.  Sollier, B.M.; Gómez, L.E.; Boix, A.V.; Miró, E.E. Oxidative coupling of methane on Sr/La$_2$O$_3$ catalysts: Improving the catalytic performance using cordierite monoliths and ceramic foams as structured substrates. *Appl. Catal. A Gen.* **2017**, *532*, 65–76. [CrossRef]

62.  Palma, V.; Pisano, D.; Martino, M. The influence of the textural properties of aluminum foams as catalyst carriers for water gas shift process. *Int. J. Hydrogen Energy* **2017**, *42*, 23517–23525. [CrossRef]

63.  Chai, R.; Zhang, Z.; Chen, P.; Zhao, G.; Liu, Y.; Lu, Y. Ni-foam-structured NiO-MO$_x$-Al$_2$O$_3$ (M = Ce or Mg) nanocomposite catalyst for high throughput catalytic partial oxidation of methane to syngas. *Microporous Mesoporous Mater.* **2017**, *253*, 123–128. [CrossRef]

64.  Méndez, F.J.; Sanz, O.; Montes, M.; Guerra, J.; Olivera-Fuentes, C.; Curbelo, S.; Brito, J.L. Selective hydrogenation of 1,3-butadiene in the presence of 1-butene under liquid phase conditions using structured catalysts. *Catal. Today* **2016**, 151–161. [CrossRef]

65.  Sanz, O.; Javier Echave, F.; Sánchez, M.; Monzón, A.; Montes, M. Aluminium foams as structured supports for volatile organic compounds (VOCs) oxidation. *Appl. Catal. A Gen.* **2008**, *340*, 125–132. [CrossRef]

66.  Ertl, G.; Knözinger, H.; Schüth, F.; Weitkamp, J. *Handbook of Heterogeneous Catalysis*, 2nd ed.; Wiley-VCH: Weinheim, Germany, 2008; ISBN 978-3-527-31241-2.

67.  Mears, D.E. Diagnostic criteria for heat transport limitations in fixed bed reactors. *J. Catal.* **1971**, *20*, 127–131. [CrossRef]

68.  Anderson, J.B. A criterion for isothermal behaviour of a catalyst pellet. *Chem. Eng. Sci.* **1963**, *18*, 147–148.

69.  Daele, T.V.; del Pozo, D.F.; Hauwermeiren, D.V.; Gernaey, K.V.; Wohlgemuth, R.; Nopens, I. A generic model-based methodology for quantification of mass transfer limitations in microreactors. *Chem. Eng. J.* **2016**, *300*, 193–208. [CrossRef]

70.  Wijaya, W.Y.; Kawasaki, S.; Watanabe, H.; Okazaki, K. Damköhler number as a descriptive parameter in methanol steam reforming and its integration with absorption heat pump system. *Appl. Energy* **2012**, *94*, 141–147. [CrossRef]

71. Liao, C.; Erickson, P.A. Characteristic time as a descriptive parameter in steam reformation hydrogen production processes. *Int. J. Hydrogen Energy* **2008**, *33*, 1652–1660. [CrossRef]

72. Talebian-Kiakalaieh, A.; Amin, N.A.S. Theoretical and experimental evaluation of mass transfer limitation in gas phase dehydration of glycerol to acrolein over supported hsiw catalyst. *J. Taiwan Inst. Chem. Eng.* **2016**, *59*, 11–17. [CrossRef]

73. Bandopadhyay, A.; Borgne, T.L.; Méheust, Y.; Dentz, M. Enhanced reaction kinetics and reactive mixing scale dynamics in mixing fronts under shear flow for arbitrary Damköhler numbers. *Adv. Water Resour.* **2017**, *100*, 78–95. [CrossRef]

74. Metkar, P.S.; Salazar, N.; Muncrief, R.; Balakotaiah, V.; Harold, M.P. Selective catalytic reduction of NO with $NH_3$ on iron zeolite monolithic catalysts: Steady-state and transient kinetics. *Appl. Catal. B Environ.* **2011**, *104*, 110–126. [CrossRef]

75. Groppi, G.; Tronconi, E. Design of novel monolith catalyst supports for gas/solid reactions with heat exchange. *Chem. Eng. Sci.* **2000**, *55*, 2161–2171. [CrossRef]

76. Boldrini, D.E.; Sánchez, M.J.F.; Tonetto, G.M.; Damiani, D.E. Monolithic stirrer reactor: Performance in the partial hydrogenation of sunflower oil. *Ind. Eng. Chem. Res.* **2012**, *51*, 12222–12232. [CrossRef]

77. Dekker, F.H.M.; Bliek, A.; Kapteijn, F.; Moulijn, J.A. Analysis of mass and heat transfer in transient experiments over heterogeneous catalysts. *Chem. Eng. Sci.* **1995**, *50*, 3573–3580. [CrossRef]

78. Hayes, R.E.; Kolaczkowskib, S.T.; Li, P.K.C.; Awdry, S. Evaluating the effective diffusivity of methane in the washcoat of a honeycomb monolith. *Appl. Catal. B Environ.* **2000**, *25*, 93–104. [CrossRef]

79. Joshi, S.Y.; Harold, M.P.; Balakotaiah, V. Overall mass transfer coefficients and controlling regimes in catalytic monoliths. *Chem. Eng. Sci.* **2010**, *65*, 1729–1747. [CrossRef]

80. Roy, P.S.; Raju, A.S.K.; Kim, K. Influence of S/C ratio and temperature on steam reforming of model biogas over a metal-foam-coated Pd–Rh/($CeZrO_2$–$Al_2O_3$) catalyst. *Fuel* **2015**, *139*, 314–320. [CrossRef]

81. Ashrafi, M.; Pröll, T.; Pfeifer, C.; Hofbauer, H. Experimental study of model biogas catalytic steam reforming: 1. Thermodynamic optimization. *Energy Fuels* **2008**, *22*, 4182–4189. [CrossRef]

82. Zeppieri, M.; Villa, P.L.; Verdone, N.; Scarsella, M.; De Filippis, P. Kinetic of methane steam reforming reaction over nickel- and rhodium-based catalysts. *Appl. Catal. A Gen.* **2010**, *387*, 147–154. [CrossRef]

83. Roh, H. Methane-reforming reactions over Ni/Ce-$ZrO_2$/θ-$Al_2O_3$ catalysts. *Appl. Catal. A Gen.* **2003**, *251*, 275–283. [CrossRef]

84. Zhang, Z.; Ding, J.; Chai, R.; Zhao, G.; Liu, Y.; Lu, Y. Oxidative dehydrogenation of ethane to ethylene: A promising $CeO_2$-$ZrO_2$-modified NiO-$Al_2O_3$/Ni-foam catalyst. *Appl. Catal. A Gen.* **2018**, *550*, 151–159. [CrossRef]

85. Mbodji, M.; Commenge, J.M.; Falk, L.; Di Marco, D.; Rossignol, F.; Prost, L.; Valentin, S.; Joly, R.; Del-Gallo, P. Steam methane reforming reaction process intensification by using a millistructured reactor: Experimental setup and model validation for global kinetic reaction rate estimation. *Chem. Eng. J.* **2012**, *207–208*, 871–884. [CrossRef]

86. Arzamendi, G.; Diéguez, P.M.; Montes, M.; Odriozola, J.A.; Sousa-Aguiar, E.F.; Gandía, L.M. Methane steam reforming in a microchannel reactor for GTL intensification: A computational fluid dynamics simulation study. *Chem. Eng. J.* **2009**, *154*, 168–173. [CrossRef]

87. Zhou, W.; Ke, Y.; Wang, Q.; Wan, S.; Lin, J.; Zhang, J.; Hui, K.S. Development of cylindrical laminated methanol steam reforming microreactor with cascading metal foams as catalyst support. *Fuel* **2017**, *191*, 46–53. [CrossRef]

88. Mbodji, M.; Commenge, J.-M.; Falk, L. Preliminary design and simulation of a microstructured reactor for production of synthesis gas by steam methane reforming. *Chem. Eng. Res. Des.* **2014**, *92*, 1728–1739. [CrossRef]

89. González-Castaño, M.; Ivanova, S.; Laguna, O.H.; Martínez, T.L.M.; Centeno, M.A.; Odriozola, J.A. Structuring Pt/$CeO_2$/$Al_2O_3$ WGS catalyst: Introduction of buffer layer. *Appl. Catal. B Environ.* **2017**, *200*, 420–427.

90. Deutschmann, O.; Schwiedemoch, R.; Maier, L.I.; Chatterjee, D. Natural gas conversion in monolithic catalysts: Interaction of chemical reactions and transport phenomena. *Stud. Surf. Sci. Catal.* **2001**, 251–258.

91. Stutz, M.J.; Poulikakos, D. Optimum washcoat thickness of a monolith reactor for syngas production by partial oxidation of methane. *Chem. Eng. Sci.* **2008**, *63*, 1761–1770. [CrossRef]

92. Montebelli, A.; Visconti, C.G.; Groppi, G.; Tronconi, E.; Kohler, S.; Venvik, H.J.; Myrstad, R. Washcoating and chemical testing of a commercial Cu/ZnO/Al$_2$O$_3$ catalyst for the methanol synthesis over copper open-cell foams. *Appl. Catal. A Gen.* **2014**, *481*, 96–103. [CrossRef]

93. Italiano, C.; Balzarotti, R.; Vita, A.; Latorrata, S.; Fabiano, C.; Pino, L.; Cristiani, C. Preparation of structured catalysts with Ni and Ni–Rh/CeO$_2$ catalytic layers for syngas production by biogas reforming processes. *Catal. Today* **2016**, *273*, 3–11. [CrossRef]

94. Cao, C.; Zhang, N.; Cheng, Y. Numerical analysis on steam methane reforming in a plate microchannel reactor: Effect of washcoat properties. *Int. J. Hydrog. Energy* **2016**, *41*, 18921–18941. [CrossRef]

95. Wójcik, S.; Ercolino, G.; Gajewska, M.; Moncada Quintero, C.M.; Specchia, S.; Kotarba, A. Robust Co$_3$O$_4$ | α–Al$_2$O$_3$ | cordierite structured catalyst for N$_2$O abatement—Validation of the SCS method for active phase synthesis and deposition. *Chem. Eng. J.* **2018**, in press.

96. Palma, V.; Pisano, D.; Martino, M.; Ciambelli, P. Structured catalysts with high thermoconductive properties for the intensification of water gas shift process. *Chem. Eng. J.* **2016**, *304*, 544–551. [CrossRef]

97. Vita, A.; Italiano, C.; Pino, L.; Laganà, M.; Recupero, V. Hydrogen-rich gas production by steam reforming of n-dodecane. Part II: Stability, regenerability and sulfur poisoning of low loading Rh-based catalyst. *Appl. Catal. B Environ.* **2017**, *218*, 317–326. [CrossRef]

98. Zhang, M.; Ning, T.; Sun, P.; Yan, Y.; Zhang, D.; Li, Z. Effect of Al$_2$O$_3$-SiO$_2$ substrate on gas-sensing properties of TiO$_2$ based lambda sensor at high temperature. *Ceram. Int.* **2018**, *44*, 3000–3004. [CrossRef]

99. Shi, R.; Shang, Y.; Zhang, Y.; Wang, P.; Zhang, A.; Yang, P. Synthesis of ultrafine α-Al$_2$O$_3$ powder by two-step hydrolysis. *Ceram. Int.* **2018**, *44*, 3741–3750. [CrossRef]